

Experimental insight into basaltic andesite lava dome oxidation textures at La Soufrière, St Vincent



Beitris Morrison-Evans*, Elena Melekhova and Jonathan Blundy

Department of Earth Sciences, University of Oxford, 3 South Parks Road, Oxford OX1 3AN, UK

BME, 0000-0001-5697-7927

*Correspondence: beitris.morrison-evans@earth.ox.ac.uk

Abstract: Petrological analysis of the 2020–21 La Soufrière lava dome reveals ubiquitous oxidation textures. Comparison of the natural dome rock to subsequent explosive scoria phases highlights the lack of any oxidation features in the latter, indicating that oxidation processes affected only the dome-forming magma, either during pre-eruptive storage or upon emplacement. To investigate the causes of oxidation we present a series of one-atmosphere experiments, using fresh natural basaltic andesite scoria as a starting material. Experiments were performed at 900 and 1020°C and at oxygen fugacities between $\text{NNO} - 2$ and air. Experimental results show that iron oxide nanolites nucleate on the rims of pyroxene microlites and phenocrysts under all experimental conditions except at $\text{NNO} - 2$. Orthopyroxene phenocrysts become unstable at 1020°C, at and above $\text{NNO} + 2$. Olivine symplectites form in all experiments at and above NNO . Titanomagnetite co-exsolves titanohematite and an Mg–Fe–Al spinel (pleonaste–magnesioferrite) at and above $\text{NNO} + 2$. Well-developed Mg–Fe–Al spinel trellis exsolution lamellae in titanomagnetite phenocrysts, as seen in the dome, only form in the presence of air at 900°C. The combination of textures and compositions observed in the natural dome indicates that oxidation of the dome magma occurred during emplacement at Earth's surface, with air percolating through the dome at temperatures $\leq 900^\circ\text{C}$.

Lava domes, ranging in composition from basaltic to rhyolitic, are the product of viscous magma extrusion at Earth's surface. Most dome-forming volcanoes experience explosive behaviour alongside effusive dome growth (Newhall and Melson 1983), from violent vent-clearing eruptions to pyroclastic density currents (PDCs) induced by dome or column collapse (Calder *et al.* 2015). Depressurization, degassing and crystallization are often invoked to explain the effusive–explosive transition at volcanoes by increasing magma viscosity (Hammer *et al.* 1999; Edmonds and Herd 2007; Bain *et al.* 2021; Utami *et al.* 2021). The mineralogy and textures observed in erupted volcanic products offer insight into these controls, for example recording the depth and conditions at which crystallization occurs (Cashman and Blundy 2000; Preece *et al.* 2013). Lava domes are often characterized by unusual alteration or groundmass textures that are absent in associated explosive phases suggesting differences in magma storage, ascent or cooling conditions (Turner *et al.* 2008; Preece *et al.* 2016). Determining the origins of these distinctive dome textures increases our understanding of where magmas reside prior to the onset of explosive activity, whether in the shallow subsurface or at Earth's surface, with implications for interpretation of geophysical signals at restless volcanoes.

Basaltic andesite lava domes have recently been identified as having the highest frequency of

associated explosive activity (Ogburn *et al.* 2015). Some of the most active basaltic andesite domes include Merapi, Indonesia (Hammer *et al.* 1999; Voight *et al.* 2000; Costa *et al.* 2013; Preece *et al.* 2013, 2016; Kelfoun *et al.* 2021), Sinabung, Indonesia (Carr 2016; Nakada *et al.* 2019), Kelud, Indonesia (Cassidy *et al.* 2019; Utami *et al.* 2021), South Soufrière Hills, Montserrat (Harford *et al.* 2002; Cassidy *et al.* 2014), La Soufrière, St Vincent (Heath *et al.* 1998; Fedele *et al.* 2021), Redoubt, Alaska (Miller 1994) and Shiveluch, Kamchatka (Dirksen *et al.* 2006; Zharinov and Demyanchuk 2013; Gorbach *et al.* 2020). The recent extrusion of a basaltic andesite lava dome, followed by a series of explosive eruptions at La Soufrière, St Vincent in 2020–21, provides a unique opportunity to study the petrological transition between the effusive and explosive stages of the eruption. This study uses experimental petrology to explore the conditions and timescales of the formation of distinctive alteration textures in the recent basaltic andesite lava dome at La Soufrière.

La Soufrière, St Vincent

The Lesser Antilles active volcanic island arc results from the relatively slow ($2\text{--}4\text{ cm a}^{-1}$; Macdonald *et al.* 2000) westward subduction of the North American plate beneath the Caribbean plate. Magma types

From: Robertson, R. E. A., Joseph, E. P., Barclay, J. and Sparks, R. S. J. (eds) 2024. *The 2020–21 Eruption of La Soufrière Volcano, St Vincent*. Geological Society, London, Special Publications, **539**, 121–152.

First published online July 17, 2023, <https://doi.org/10.1144/SP539-2022-298>

© 2023 The Author(s). This is an Open Access article distributed under the terms of the Creative Commons Attribution License (<http://creativecommons.org/licenses/by/4.0/>). Published by The Geological Society of London.

Publishing disclaimer: www.geolsoc.org.uk/pub_ethics

Table 1. Whole-rock compositions of dome and U3 scoria

	Dome*		Scoria*		
	average	sd	LS21-38a [†]	average U3	sd
SiO ₂	54.68	0.23	53.92	53.75	0.49
TiO ₂	1.01	0.02	0.97	0.95	0.03
Al ₂ O ₃	17.79	0.1	18.38	18.52	0.37
FeO*	8.33	0.13	8.31	8.25	0.23
MnO	0.21	0	0.2	0.19	0.01
MgO	3.73	0.08	3.84	4.19	0.34
CaO	8.38	0.08	8.81	8.93	0.12
Na ₂ O	3.33	0.05	3.19	3.27	0.07
K ₂ O	0.58	0.01	0.56	0.54	0.02
P ₂ O ₅	0.13	0	0.13	0.13	0.01
Sum	98.17		98.31	98.72	
<i>n</i>	8			9	

*Analysed using XRF by [Weber *et al.* \(2023\)](#).

[†]Starting material used in this study.

n is number of analyses; sd is standard deviation.

along the arc range from high-Mg basalts through basaltic andesites and andesites to dacites ([Brown *et al.* 1977](#); [Macdonald *et al.* 2000](#)), with compositions typical of oceanic arcs worldwide. Rhyolitic magmas are exceedingly rare. Eruption styles range from effusive lava flows and domes, to explosive Plinian and sub-Plinian eruptions and phreatic events. There are currently around 21 active volcanic centres along the arc ([Fedele *et al.* 2021](#)).

La Soufrière is the active volcanic centre on the island of St Vincent. Magmas and pyroclastic material range from basaltic (ol + cpx + plag + sp) to basaltic andesite (plag + cpx + opx + tmt ± ol). La Soufrière volcano erupts predominantly basaltic andesite, with only some eruptions producing silica-undersaturated high-Mg basalt ([Heath *et al.* 1998](#); [Cole *et al.* 2019](#)). La Soufrière has seen six major historical eruptions: 1718, 1812, 1902–03, 1971–72, 1979, 2020–21.

The most recent 2020–21 eruption of La Soufrière began in late December 2020 with the extrusion of a basaltic andesite dome in the crater SW of the remnant 1979 dome with minimal precursory seismicity ([Joseph *et al.* 2022](#)). Fresh dome samples were collected by the University of the West Indies Seismic Research Centre (UWI-SRC) team on 16 January 2021, twenty days after the dome first breached the surface. Footprints of the expanding dome illustrate growth c. 150 m NW and c. 100 m SE by the time of sampling ([Joseph *et al.* 2022](#)). By February 2021 the dome had elongated to become a coulée, confined between the remnant 1979 dome and the crater wall. Subsequently a series of five explosive eruptions (U1–U5; [Cole *et al.* 2023](#)) commenced in early April 2021, destroying the 2020 and 1979 domes, and causing numerous

PDCs and lahars. Samples from the explosive phase were collected on 11 April from multiple locations around the flanks of the volcano ([Cole *et al.* 2023](#); [Weber *et al.* 2023](#)). The bulk chemical composition of both the effusive and explosive stages of this eruption are near-identical ([Table 1](#)); however, the erupted rocks themselves are texturally distinct. Two-pyroxene thermobarometry indicates magmatic temperatures of 900–1020°C, with the scoria temperatures slightly higher than the dome ([Weber *et al.* 2023](#)). The surface temperature of the dome, measured using a FLIR T65osc thermal camera in January 2021, gave readings of 590 ± 12°C, where rockfalls had exposed the interior of the dome ([Stinton 2023](#)), highlighting significant cooling upon eruption and a thermal gradient from the centre to the edge of the dome.

Lava dome petrology overview

Detailed petrological analyses of lava domes provide essential information on dome crystallinity ([Swanson *et al.* 1987](#); [Fink *et al.* 1990](#)), rate of extrusion ([Walker *et al.* 1973](#); [Huppert *et al.* 1982](#); [Fink and Griffiths 1998](#)), magma temperature and oxidation state ([Pallister *et al.* 2008](#); [Ridolfi *et al.* 2010](#); [Costa *et al.* 2013](#); [Laeger *et al.* 2013](#); [Grocke *et al.* 2016](#)), and porosity and permeability ([Colombier *et al.* 2017](#); [Heap *et al.* 2019](#); [Darmawan *et al.* 2022](#)). Petrological studies documenting the alteration and mineral breakdown textures often observed in lava domes allude to high-temperature sub-solidus oxidation during dome growth at Earth's surface due to, for example, interaction with the atmosphere or groundwater ([Von Gruenewaldt *et al.* 1985](#); [Saito](#)

et al. 2004a; Turner *et al.* 2008). Lava domes are characteristically microlite-rich (Preece *et al.* 2013; Murch and Cole 2019) and exhibit the breakdown of certain minerals, such as amphibole (Genareau and Clarke 2010; Ludlam *et al.* 2018; Gorbach *et al.* 2020), Fe–Ti oxides (Saito *et al.* 2004a, b, 2007) and olivine (Weber *et al.* 2023). There is a paucity of published literature regarding the simultaneous breakdown of co-existing mineral phases, as seen in natural dome rocks, over a range of physico-chemical conditions. In such cases, breakdown or alteration reactions of different phases may operate in tandem. Subsequent explosive phases of similar magma during the same eruptions often appear unaltered and are instead highly vesicular and more glassy (Hammer *et al.* 1999). In such cases the textural differences between effusive and explosive phases can be used to distinguish the eruptive style and provide insight into changing magma ascent, storage and eruption conditions.

Experimental studies complement petrological findings by providing constraints on the mechanisms and timescales over which dome-rock mineralogy and textures form. Heating and oxidation experiments using natural samples elucidate dome-forming processes, finding that sustained high temperatures play a significant role in facilitating sub-solidus oxidation at Earth's surface (Vincent *et al.* 1957; Buddington and Lindsley 1964; Haggerty and Baker 1967; Haggerty 1976a; D'Oriano *et al.* 2013, 2014; Knafelc *et al.* 2019). Synthetic experiments supplement those using natural starting materials by further constraining the stability fields of specific minerals, in pressure, temperature, and oxygen fugacity (P–T– f_{O_2}) space (Turnock and Eugster 1962; Speidel 1967; Woermann *et al.* 1969; Freer and Hauptman 1978; Sack 1982; Harrison and Putnis 1998). Comparison of experimentally produced exsolution textures and compositions to those in natural samples are used in this study to identify the magmatic conditions and timescales at which oxidation occurred, and hence infer the likely mechanism responsible.

Oxidation mechanisms

Extruded magmas undergo oxidation at or near the Earth's surface by three main end-member processes: hydrothermal alteration (Ball *et al.* 2013, 2015; Heap *et al.* 2019; Darmawan *et al.* 2022); interaction with air (Saito *et al.* 2004a; Burkhard 2005a); or deuteritic alteration (Hekinian 1982; Burgisser and Scaillet 2007). Of these mechanisms, the first two are considered exogenous, and the third exogenous in terms of the source of the oxidizing agent. The processes are not mutually exclusive and may operate in tandem or sequentially. There may be spatial heterogeneity in the extent to which

different processes operate, for example with greater oxidation at the sample surface and greater deuteritic alteration in the interior.

Hydrothermal alteration involves interactions between magma and high temperature fluids (<500°C; Darmawan *et al.* 2022) that may be meteoric, seawater, groundwater or surficial (e.g. crater lake) in origin (Ball *et al.* 2013). Oxidation of primary magmatic minerals to form hydrothermal alteration textures and deposit secondary hydrous minerals such as clays (Ball *et al.* 2015) typically occurs on timescales of months to years (Heap *et al.* 2019).

Lava emplaced at the Earth's surface inevitably interacts with the atmosphere and consequently can become oxidized. High temperatures are required for such oxidation reactions to be kinetically feasible on eruption timescales (Burkhard 2001, 2005a). Examples of maintained heat sources at the Earth's surface include lava lakes, growing lava domes, or the extrusion of successive lava lobes (Saito *et al.* 2004a; Burkhard 2005a, b). The ability of air to penetrate into extruding magma, via pore spaces or growing microfractures, controls the pervasiveness of the oxidation observed (Colombier *et al.* 2017). Thus, oxidation is more likely to affect the exposed exterior surface of domes rather than their interiors.

Deuteritic alteration involves the auto-oxidation (or reduction) of a magma by volatile species (e.g. H_2O or SO_2) produced by the magma itself, either during degassing or crystallization (Sato and Wright 1966; Mathez 1984; Holloway 2004; Burgisser and Scaillet 2007). The composition and mass of exsolved water and sulfur in an ascending magma determines the extent of oxidation or reduction of up to $\pm 2 \log f_{O_2}$ units (Anderson and Wright 1972; Hekinian 1982; Carmichael and Ghiorso 1986; Burgisser and Scaillet 2007). The fact that both oxidation and reduction can occur reflects the different speciation and solubility of fluids, such as H_2 , H_2S and SO_2 , in fluids and melts. Deuteritic alteration tends to effect pore spaces, volcanic glass and interstices between crystals, often recorded by zoning and exsolution around the rims of iron–titanium oxide minerals (Duchesne 1972), and can occur either at the Earth's surface or during sub-surface storage and cooling, for example in volcanic conduits. Gas streaming, whereby fluids released from deeper parts of the same magmatic system interact with hot, extruded magma, may also be considered a variant of deuteritic alteration.

Iron–titanium oxides

Fe–Ti oxides and olivines are typically the first minerals to crystallize at the liquidus of basaltic magmas, hence they may become unstable in the presence of melt at low temperatures and can readily oxidize

at Earth's surface (Haggerty and Baker 1967; Woermann *et al.* 1969; Goode 1974; Nitsan 1974; Haggerty 1976a, b). The structure and composition of Fe–Ti oxides varies widely, with the ulvöspinel ($\text{Fe}_2\text{-TiO}_4$)–magnetite (Fe_3O_4) solid solution (usp–mnt) particularly common in volcanic rocks, along with the spinel (MgAl_2O_4)–hercynite (FeAl_2O_4) and pleonaste ($\text{Mg}_x\text{Fe}_{1-x}\text{Al}_2\text{O}_4$)–magnesioferrite (MgFe_2O_4) solid solutions. In more evolved magmas it is the ilmenite (FeTiO_3)–hematite (Fe_2O_3) solid solution (ilm–hmt) that becomes predominant (Haggerty 1976a, b). The terms ‘titanomagnetite’ and ‘titano hematite’ are commonly used, as here, to refer to intermediate oxides within the usp–mnt and ilm–hmt solid solutions, respectively (Buddington and Lindsley 1964).

Co-existing titanomagnetite and titano hematite pairs are frequently used as thermo-oxybarometers to estimate the temperature and oxidation state (expressed as $f\text{O}_2$) of a magma prior to eruption (Buddington and Lindsley 1964; Frost and Lindsley 1991). Fe–Ti oxides re-equilibrate relatively quickly (<100 h; Freer and Hauptman 1978; Gardner *et al.* 1995; Venezky and Rutherford 1999; Hou *et al.* 2021) to changes in P–T– $f\text{O}_2$, and thus record the most recent magmatic conditions experienced, including slow, sub-solidus cooling in some cases (Hammond and Taylor 1982). During re-equilibration, Fe–Ti oxides may undergo exsolution, with different exsolving phases and textures dependent on the initial grain composition and new P–T– $f\text{O}_2$ conditions (Nickel 1958). One of the challenges in interpreting oxide exsolution features is the many solid-solutions and potential exsolution mechanisms involved (Arguin *et al.* 2018).

Previous heating and oxidation experiments using naturally exsolved Fe–Ti oxides explore the re-homogenization of exsolution features (Vincent *et al.* 1957; Nickel 1958; Price 1980), the diffusivity of cations between phases and their associated activation energies (Creer *et al.* 1970; Petersen 1970; Freer and Hauptman 1978; Price and Putnis 1979; Freer and O'Reilly 1980; Price 1981), the influence of Mg, Al, Cr, Mn, Zn substitutions (Sack 1982; Von Gruenewaldt *et al.* 1985; Lattard 1995) and solid solution solvus temperatures (Vincent *et al.* 1957; Turnock and Eugster 1962; Woermann *et al.* 1969; Muan *et al.* 1972; Frost 1991; Harrison and Putnis 1998; Tan *et al.* 2016). However, few studies investigate the exsolution of numerous co-existing oxide phases from complex solid solutions in natural rocks.

Olivine

Olivine is generally confined to lava domes with more primitive basaltic andesite compositions (e.g. Merapi, Costa *et al.* 2013; Arenal, Reagan *et al.*

1987; Kelud, Utami *et al.* 2021; St Vincent, Weber *et al.* 2023). Olivine is unstable in the presence of melt at low temperatures (<1180°C at 1 atm; Nicholls and Ringwood 1973), thus may break down during ascent, eruption and cooling at Earth's surface (Champness 1970; Goode 1974; Nitsan 1974; Moore *et al.* 2022). Olivine symplectites (vermicular exsolution textures) form by either discontinuous or continuous breakdown, producing intergrowths of either orthopyroxene and magnetite (discontinuous), or high-forsterite (Fo) olivine and hematite (continuous) (Johnston and Stout 1984; Del Moro *et al.* 2013). Analyses of natural olivine symplectites found the composition of exsolved phases to depend on the forsterite content of the initial olivine crystals (Moseley 1984; Ejima *et al.* 2013, 2017), and whether exsolution occurred by atmospheric oxidation (Haggerty 1976a; Gualtieri *et al.* 2003; Knafelc *et al.* 2019) or by magma mixing (Ueki *et al.* 2020). High degrees of oxidation can produce rims of Fe-oxides along grain boundaries, of variable thickness, known as oxide diffusion rims. Such rims reflect the efficient diffusion and subsequent oxidation of iron from the host olivine crystal. They are often composed of hematite in association with Fe-depleted adjacent olivine (Haggerty and Baker 1967). Previous experimental studies also highlight the temperature dependence of the extent of olivine exsolution (Knafelc *et al.* 2019; Moore *et al.* 2022).

Pyroxene

Orthopyroxene and clinopyroxene are common in basaltic andesite magmas. The composition of two co-existing pyroxene phases can be used to determine crystallization temperatures by two-pyroxene thermometry (Wells 1977; Lindsley and Andersen 1983; Putirka 2008). Slow cooling may result in pyroxenes undergoing sub-solvus exsolution, skewing thermometry estimates; but instead providing new, reset values for equilibration temperatures (Kuno 1966; Longhi and Bertka 1996). Orthopyroxene and clinopyroxene are stable over different P–T ranges, often determined experimentally (Kuno 1966; Grove and Juster 1989; Canil 1994). Pyroxenes can also form as reaction products from the oxidation and breakdown of olivine (Johnston and Stout 1984; Barton and Van Gaans 1988; Barton *et al.* 1991), garnet (Ringwood and Lovering 1970), and clinopyroxene (Boland and Otten 1985).

Methods and materials

Experimental methods

The starting material selected for this experimental study is a basaltic andesite scoria from the 2020–21 eruption at La Soufrière, St Vincent. The scoria

(LS21-38a) is from the U3 phase (see [Cole et al. 2023](#) for further details) of the explosive sequence and was collected hot in April 2021. The bulk chemical compositions of the dome and scoria from this eruption are very similar (Table 1) and both contain the same phenocryst assemblage (plag + cpx + opx + tmt \pm ol), although microlite assemblages differ (Table 2; [Frey et al. 2023](#); [Weber et al. 2023](#)). The scoria provides a sample of the 2020–21 magma that quenched rapidly, thus remaining fresh and unmodified by surface processes. By subjecting this magma to different experimental conditions, we aim to explore whether the dome- and scoria-forming magmas could plausibly be derived from similar batches of basaltic andesite magma that experienced distinctive surface and near-surface conditions, giving rise to the observed textural differences.

The LS21-38a scoria was lightly crushed in an agate mortar, allowing phenocrysts to be preserved and only the interstitial groundmass to become powdered and disaggregated. This technique enables new microlites to grow in the groundmass, if run for sufficient time, and facilitates reactions between phenocrysts and the interstitial reactive melt during experimental runs ([Cassidy et al. 2019](#)). The crushed scoria was mixed with PVA glue as a binder and loaded onto thin platinum (Pt) wire loops. The Pt wire was later analysed to ensure that no Fe-loss had occurred. In total, we report eight one-atmosphere experiments, carried out in a vertical furnace and air-quenched, each at a different fO_2 and temperature (Table 3). Oxygen fugacity was set using a CO₂–CO gas mix ([Deines et al. 1976](#)) and calibrated before each experiment using an yttria-doped zirconia probe and the Nernst equation ([Boullong et al. 2020](#)). Experiments run in air did not require fO_2 calibration. The temperature was set with a Eurotherm temperature controller and calibrated to the melting point of gold using a type-B thermocouple at the furnace hotspot. Charges were lowered into the hot zone of the furnace and run for the duration of a week, to facilitate chemical exchange ([Freer and Hauptman 1978](#); [Cottrell et al. 1999](#)) on a comparable timescale to that experienced by the natural dome at the surface.

Subduction zone magmas, such as those from St Vincent, have oxidation states in their sources between NNO – 2 and NNO + 2 ([Carmichael 1991](#); [Cashman 1992](#); [Heath et al. 1998](#)), where NNO denotes the nickel–bunsenite reference curve at the P–T of interest, typically becoming more oxidized upon eruption as they crystallize and degas ([Mathez 1984](#); [Burgisser and Scaillet 2007](#)). Basaltic andesite eruption temperatures are typically in the range of 1000 to 1200°C, depending on initial volatile content and ascent trajectory through P–T space ([Gaetani et al. 1994](#); [Moore and Carmichael 1998](#)). Estimates of the eruption temperature of the 2020–

21 St Vincent basaltic andesites, based on two-pyroxene thermometry, are in the range *c.* 900–1020°C ([Weber et al. 2023](#)). The estimated fO_2 for similar historical magmas are in the range of NNO to NNO + 1 ([Heath et al. 1998](#)). The one-atmosphere basaltic andesite solidus under anhydrous (fully degassed) conditions is at or slightly below 900°C ([Schiavi et al. 2009](#)). Therefore, experimental conditions chosen here include temperatures of 900 and 1020°C; oxygen fugacities of NNO – 2, NNO, NNO + 2 and air; and run durations of a week, each to allow for comparison with the natural dome that extruded at the surface less than twenty days prior to sampling.

Analytical methods

Experimental run products were mounted in epoxy, polished and analysed on a Cameca SX-5 FE electron microprobe at the Department of Earth Sciences, University of Oxford. Phenocrysts and microlites were analysed with a focused beam, at an accelerating potential of 15 keV and beam current of 20 nA (10 nA for microlites). Secondary standards include SJI olivine, labradorite and glass (T1, GOR128 and KL2G). Total iron was determined as Fe²⁺ (FeO^T). For iron oxides containing Fe in more than one valence state, FeO^T was recalculated to Fe²⁺ and Fe³⁺ on the basis of stoichiometry and checked by charge balance. Oxides were normalized to 32 oxygens, those with 21 cations forming part of the rhombohedral oxide group and those with 24 cations the cubic oxide group. High-resolution backscattered electron (BSE) images were acquired using the Zeiss Merlin (field emission gun – FEG) and Zeiss Evo (tungsten filament) scanning electron microscopes (SEMs) at the Department of Materials, University of Oxford. Analytical conditions were 20 keV accelerating potential and 5 nA beam current. Thin sections of the dome (SV3) and scoria (LS21-38a) rock samples were also imaged on the SEM using the same analytical conditions. Chemical analyses of the natural dome and scoria samples were carried out by [Frey et al. \(2023\)](#) and [Weber et al. \(2023\)](#). Representative analyses of whole-rocks and minerals are presented in Tables 1 and 2, respectively.

2020–21 La Soufrière lava dome and scoria

Both the effusive dome and explosive scoria phases of the 2020–21 eruption have a basaltic andesite bulk composition, with 45–50 vol% phenocrysts in a microlite-rich or vesicular groundmass, respectively. Phenocrysts (vol% from [Weber et al. 2023](#)), in order of abundance, are plagioclase (An 60–86; *c.* 26 vol%), orthopyroxene (Mg# 67–70; *c.* 8 vol%),

Table 2. Representative mineral compositions in dome and U3 scoria

		Dome	TiO ₂	Al ₂ O ₃	FeO*	MnO	MgO	CaO	Na ₂ O	K ₂ O	P ₂ O ₅	Total	Fo	An	En	Mg#	Fe ³⁺ #	Ti pfu
Plagioclase	microlite UZ [†]	56.91	0.08	26.91	1.04	bd	0.15	9.75	5.73	0.14	bd	100.71		48				
	microlite core [†]	49.50	0.03	31.85	0.74	bd	0.03	15.39	2.87	0.04	bd	100.43		75				
	microlite rim [†]	55.78	0.06	27.88	0.83	bd	0.05	10.34	5.50	0.14	bd	100.58		51				
	phenocryst core*	47.05	0.01	33.86	0.67	na	0.07	17.41	1.66	0.02	na	100.75		85				
	phenocryst rim*	52.78	0.04	30.17	0.55	na	0.04	12.84	4.23	0.06	na	100.72		62				
Orthopyroxene	microlite [†]	52.62	0.39	1.58	21.02	bd	21.49	1.99	bd	bd	bd	99.08			62	65		
	phenocryst core*	53.47	0.25	0.80	19.89	0.75	23.60	1.80	bd	bd	bd	100.65			65	68		
	phenocryst rim*	53.51	0.28	1.17	18.82	0.74	23.68	1.95	bd	bd	bd	100.22			66	69		
Clinopyroxene	microlite [†]	52.49	0.49	1.28	12.02	bd	15.43	17.52	0.20	0.00	na	100.02			45	70		
	phenocryst core*	51.86	0.58	1.82	9.62	0.34	14.85	20.46	0.28	0.01	na	99.82			42	73		
	phenocryst rim*	51.61	0.65	2.32	10.71	0.45	14.46	19.94	0.30	0.00	na	100.45			42	71		
Olivine	microlite [†]	na	na	na	na	na	na	na	na	na	na							
	phenocryst core*	38.38	na	na	23.26	0.45	38.70	0.14	na	na	na	100.97	74					
	phenocryst rim*	39.53	na	na	17.01	0.43	44.04	0.14	na	na	na	101.17	82					
Fe–Ti oxide ox1	microlite [†]	0.14	15.19	0.74	70.22	0.58	3.99	0.11	bd	na	na	90.96				22	91	0.7
	host1*	0.41	16.54	1.91	67.72	0.36	2.61	bd	bd	bd	bd	89.54				10	91	0.5
	exsolved 1	0.10	1.99	10.64	69.13	1.59	7.40	bd	bd	bd	bd	90.86				39	76	0.1
ox2	host2	0.07	5.22	4.66	78.47	0.74	3.63	bd	bd	bd	bd	92.79				18	88	0.1
	exsolved2	0.03	24.91	0.82	64.56	0.26	2.30	bd	bd	bd	bd	92.89				18	98	0.5
ox3 [‡]	host3	0.03	9.52	2.86	78.07	0.26	1.62	bd	bd	bd	bd	92.36				7	91	0.3
	exsolved3a	0.03	0.12	6.50	76.02	2.14	9.55	bd	bd	bd	bd	94.36				46	86	0.0
	exsolved3b	0.00	0.22	4.51	83.71	0.70	2.33	bd	bd	bd	bd	91.48				13	90	0.0
	exsolved3c	0.06	0.02	0.49	89.20	0.02	0.03	bd	bd	bd	bd	89.81				0	99	0.0
ox4	host4*	0.08	9.00	3.12	74.66	0.51	2.63	bd	bd	bd	bd	90.00				12	90	0.3
	exsolved4*	0.02	28.01	0.55	59.02	0.29	2.45	bd	bd	bd	bd	90.35				18	98	0.6

		U3 Scoria	TiO ₂	Al ₂ O ₃	FeO*	MnO	MgO	CaO	Na ₂ O	K ₂ O	P ₂ O ₅	Total	Fo	An	En	Mg#	Fe ³⁺ #	Ti pfu
		SiO ₂																
Plagioclase	microlite UZ [†]	54.39	0.06	28.17	0.79	bd	0.08	10.96	5.07	0.10	bd	99.63		54				
	microlite core [†]	48.07	0.03	32.36	0.75	bd	0.05	15.90	2.33	0.03	bd	99.51		79				
	microlite rim [†]	53.96	0.05	28.44	0.74	bd	0.08	11.38	4.92	0.09	bd	99.64		56				
	phenocryst core*	46.16	0.03	33.75	0.61	na	0.06	17.74	1.52	0.02	na	99.92		86				
	phenocryst rim*	53.35	0.03	28.95	0.52	na	0.08	12.33	4.54	0.08	na	99.88		60				
Orthopyroxene	opx microlite [†]	53.73	0.15	0.55	19.41	bd	22.89	2.73	0.04	0.00	na	99.51			64	70		
	int-pyx microlite [†]	51.20	0.51	2.12	18.07	bd	19.49	8.13	0.15	0.00	na	99.67			58	68		
	phenocryst core*	52.40	0.36	1.45	18.72	0.58	24.41	1.85	0.04	0.00	na	99.88			67	70		
	phenocryst rim*	52.88	0.27	1.02	20.11	0.76	22.61	1.63	0.00	0.00	na	99.28			64	67		
Clinopyroxene	microlite [†]	49.23	1.28	5.08	10.43	bd	13.51	20.27	0.34	0.00	na	100.13			41	75		
	phenocryst core*	51.59	0.54	1.64	10.62	0.44	14.77	19.81	0.31	0.00	na	99.70			42	71		
	phenocryst rim*	52.15	0.53	1.81	10.32	0.48	14.61	20.05	0.24	0.00	na	100.18			42	72		
Olivine	microlite [†]	37.87	na	0.02	25.07	0.49	35.72	0.23	na	na	na	99.40	71					
	phenocryst 1*	36.44	na	na	30.48	0.61	32.19	0.16	na	na	na	99.93	65					
	phenocryst 2*	38.32	na	na	22.87	0.41	38.79	0.15	na	na	na	100.60	75					
Fe–Ti oxide	microlite [†]	0.16	14.11	2.86	73.14	0.54	2.15	0.12	bd	na	na	93.07				12	71	0.6
	host 1*	0.08	13.39	3.31	74.91	0.53	2.81	bd	bd	bd	bd	95.03				11	88	0.4
	host 2*	0.05	6.98	5.99	76.53	0.33	3.87	bd	bd	bd	bd	93.75				18	84	0.2

Forsterite content (Fo) calculated as mol% Mg/(Mg + Fe + Mn); Anorthite content (An) as mol% Ca/(Ca + Na); Enstatite content (En) as mol% Mg/(Mg + Fe²⁺ + Mn + Ca); Mg# as cation fraction (Mg²⁺/(Mg²⁺ + Fe²⁺)); Fe³⁺ # as cation fraction (Fe³⁺/(Fe³⁺ + Al³⁺)); and Titanium as cations per formula unit (Ti pfu). UZ is unzoned microlite.

*Analysed using EPMA by [Weber et al. \(2023\)](#).

[†]Analysed using EPMA by [Frey et al. \(2023\)](#).

*See Figure 1f.

Table 3. *Experimental run conditions and products*

Run #	Temperature (°C)	<i>f</i> O ₂	Duration (hours)	Phases present	plag			opx		cpx	
					phenocryst core An	phenocryst rim An	microlite An	phenocryst Mg#	microlite Mg#	phenocryst Mg#	microlite Mg#
SV31	1020	AIR	161	gl, plag, opx, cpx, ol, tmt, tht	89 (6)	62 (2)	51 (7)	88–93*	na	72 (1)	83 (2)
SV27	900	AIR	161	gl, plag, opx, cpx, ol, tmt, tht, spn	83 (7)	65 (4)	46 (5)	68 (1)	61 (4)	71 (5)	na
SV22	1020	NNO + 2	165	gl, plag, opx, cpx, ol, tmt, tht, spn	92 (1)	66 (8)	51	73	86	75 (1)	75 (1)
SV33	900	NNO + 2	166	gl, plag, opx, cpx, ol, tmt, tht, spn	82 (2)	64 (2)	44 (5)	70 (1)	65 (3)	72 (2)	na
SV25	1020	NNO	168	gl, plag, opx, cpx, ol, tmt	84	51	45 (0.2)	71 (2)–78*	na	76	76
SV32	900	NNO	161	gl, plag, opx, cpx, ol, tmt, tht	93	59 (2)	48	69 (3)	59 (3)	72 (3)	70 (0.02)
SV29	1020	NNO – 2	144	gl, plag, opx, cpx, ol	88 (6)	66 (8)	82 (0.01)–53 (2)†	68	64 (2)	71 (1)	na
SV28	900	NNO – 2	161	gl, plag, opx, cpx, tmt, tht	74 (12)	60 (2)	80–50 (6)†	na	59 (4)	72 (1)	67

Phases present: gl, glass; plag, plagioclase; opx, orthopyroxene; cpx, clinopyroxene; ol, olivine; tmt, titanomagnetite; tht, titanohematite; spn, Mg–Fe–Al spinel. Abbreviations include: na, not analysed; bd, below detection.

Units in parentheses are standard deviations of average phase compositions; exsolution textural terms after Haggerty (1976a).

*Analyses of unaltered core (low Mg#) and altered rim (high Mg#).

†Average core and rim values of zoned plagioclase microlites.

‡Ti pfu std <0.01.

clinopyroxene (Mg# 71–73; *c.* 6 vol%), titanomagnetite (Ti pfu 0–0.6; Mg# 0–46; *c.* 5 vol%) and olivine, which is notably more rare in the dome than the scoria (Fo 74–75; 0.5 vs 2 vol%; Table 2). Although phenocryst phase assemblages and bulk compositions in the dome and scoria are almost identical, the phenocrysts in the dome are texturally distinct to those in the erupted scoria. Dome textures are suggestive of breakdown reactions of mineral phases originally co-existing with melt in the dome-forming magma (Fig. 1, and shown in Joseph *et al.* 2022). The lack of such textures in the scoria highlights the difference in eruptive conditions (*sensu lato*) between the two stages of the eruption. Microlite assemblages in the dome (plag + opx + ox) and scoria (plag + opx + cpx ± ol ± ox) units are also different (Frey *et al.* 2023).

Textural differences

Microlites. The scoria groundmass is vesicular and glassy, with swallow-tail and acicular microlites (1–30 µm; Cashman 1992) of dominantly plagioclase and pyroxene (Fig. 1a). The groundmass of the dome is instead more crystalline with microlites appearing slightly larger than those in the scoria (Fig. 1b) and composed of laths of plagioclase and pyroxenes rimmed with oxide nanolites (defined as microcrystals <1 µm in size; Mujin *et al.* 2017).

Oxide microlites and nanolites are more abundant in the dome.

Pyroxene phenocrysts. Orthopyroxene and clinopyroxene phenocrysts in the scoria and dome are subhedral, fractured, and contain inclusions of oxides and melt (Fig. 1c, d). In the dome, orthopyroxene phenocrysts are rimmed with iron oxide nanolites (Fig. 1d), similar to those seen around the pyroxene microlites. There are no obvious alteration textures seen in clinopyroxene.

Iron–titanium oxide phenocrysts. Titanomagnetites in the scoria are homogenous with no evidence of exsolution (Fig. 1e). Fe–Ti oxides in the dome, on the other hand, are significantly altered, displaying a range of exsolution textures. Four different styles of exsolution are observed (Fig. 1f) and are described following Buddington and Lindsley (1964) and Haggerty’s (1976a) classification schemes: cloth-like, sandwich-type, trellis lamellae, and recrystallization granules. These oxide exsolution textures observed in oxides 1–4 are described in the subsequent discussion. Oxide 1 illustrates well-developed coarse trellis lamellae along two planes, forming exsolution cells in the centre of the grain. Oxide 2 displays ‘sandwich-type’ lamellae, with irregular exsolution bands. Oxide 3, previously connected to oxide 1 as evidenced by their irregular adjacent

ol phenocryst Fo	tmt host			tht exsolved			spn			Fe–Ti oxide exsolution textures
	Mg#	Fe ³⁺ #	Ti pfu	Mg#	Fe ³⁺ #	Ti pfu	Mg#	Fe ³⁺ #	Ti pfu [‡]	
97 (1)	16 (6)	95 (3)	0.3	13 (1)	91 (6)	0.7	–	–	–	Vermicular
94 (1)	7 (2)	92 (1)	0.2	12 (2)	80 (10)	0.7	54 (4)	69 (4)	bd	Coarse regular trellis lamellae (spn), vermicular and recrystallized (tht)
92 (0.3)	12 (0.2)	92 (0.3)	0.4	15 (0.3)	83 (2)	0.7	39 (2)	85 (0.3)	bd	Sandwich type (spn) and granules at edge (tht)
85 (3)	9 (2)	91 (2)	0.5	15 (0.6)	73 (5)	0.8	22 (1)	85 (1)	0.1	Sandwich type (spn) and granules at edge (tht)
83 (0.01)	27 (1)	93 (0.01)	0.2	–	–	–	12 (0.1)	95 (0.2)	0.6	Sandwich type
96 (0.1)	6 (1)	93 (1)	0.4	7 (5)	84 (1)	0.73	–	–	–	Sandwich type
55 (0.1)	–	–	–	–	–	–	–	–	–	
–	6	86	0.4	7	96	0.6	–	–	–	

grain boundaries, is dominated by recrystallized external granules of a white (high-Z) phase in the BSE image and contains pockets of a dark grey (low-Z) phase displaying fine cloth-like exsolution lamellae along three different planes (Fig. 1f inset). Cloth-like exsolution textures are usually associated with sub-solvus exsolution (<600°C; Arguin *et al.* 2018) and could represent further exsolution during cooling. Oxide 4 (not shown) is similar to oxide 2 in that it forms irregular ‘sandwich type’ lamellae, but predominantly along grain boundaries and fractures.

Olivine phenocrysts. As noted above, olivine is significantly more abundant in the scoria than in the dome. Scoria olivine forms subhedral homogenous phenocrysts, with fractures and sometimes containing oxide or melt inclusions (Fig. 1g). Olivines in the dome are rarer, and those identified are heavily altered, with symplectitic exsolution occurring predominantly along grain boundaries and fractures (Fig. 1h). Symplectites extend inwards towards the centre of the crystal and appear to grow as fibrous lobes, previously described as ‘budding’ (Haggerty and Baker 1967).

Compositional differences

Microlites. Plagioclase microlites in the scoria have a slightly higher anorthite content than those in the

dome, for example An 56–79 (dome) and An 51–75 (scoria) in terms of rim–core values (Table 2; Frey *et al.* 2023). Conversely, pyroxene microlites appear to be compositionally similar in both the dome and scoria (opx Mg# 67–69; cpx Mg# 76–78). Oxide microlites are more abundant in the dome and are ulvöspinel-rich (higher Ti and Fe²⁺) compared to the few oxide microlites in the scoria (5.4 vol% v. 0.2–0.9 vol%; Frey *et al.* 2023); with both containing minor concentrations of MgO (<6 wt%) and Al₂O₃ (<6 wt%). Olivine microlites in the scoria range from Fo68 to Fo74; no olivine microlites were identified in the dome.

Pyroxene phenocrysts. Both the orthopyroxene (Mg# 67–70) and clinopyroxene (Mg# 71–73) phenocrysts in the dome and scoria are compositionally very similar, with little titanium and aluminium present (<0.4 wt% TiO₂ and <1.5 wt% Al₂O₃ in orthopyroxene and <0.7 wt% TiO₂ and <2.3 wt% Al₂O₃ in clinopyroxene; Table 2). There is no sign of zoning or compositional variation from crystal cores to rims.

Iron–titanium oxide phenocrysts. Two distinct oxide compositions are found in the scoria, one ulvöspinel-rich (higher Ti and Fe²⁺) and one magnetite-rich (higher Fe³⁺, Mg, and Al; Table 2). Variation in Fe–Ti oxide compositions is typical in island-arc

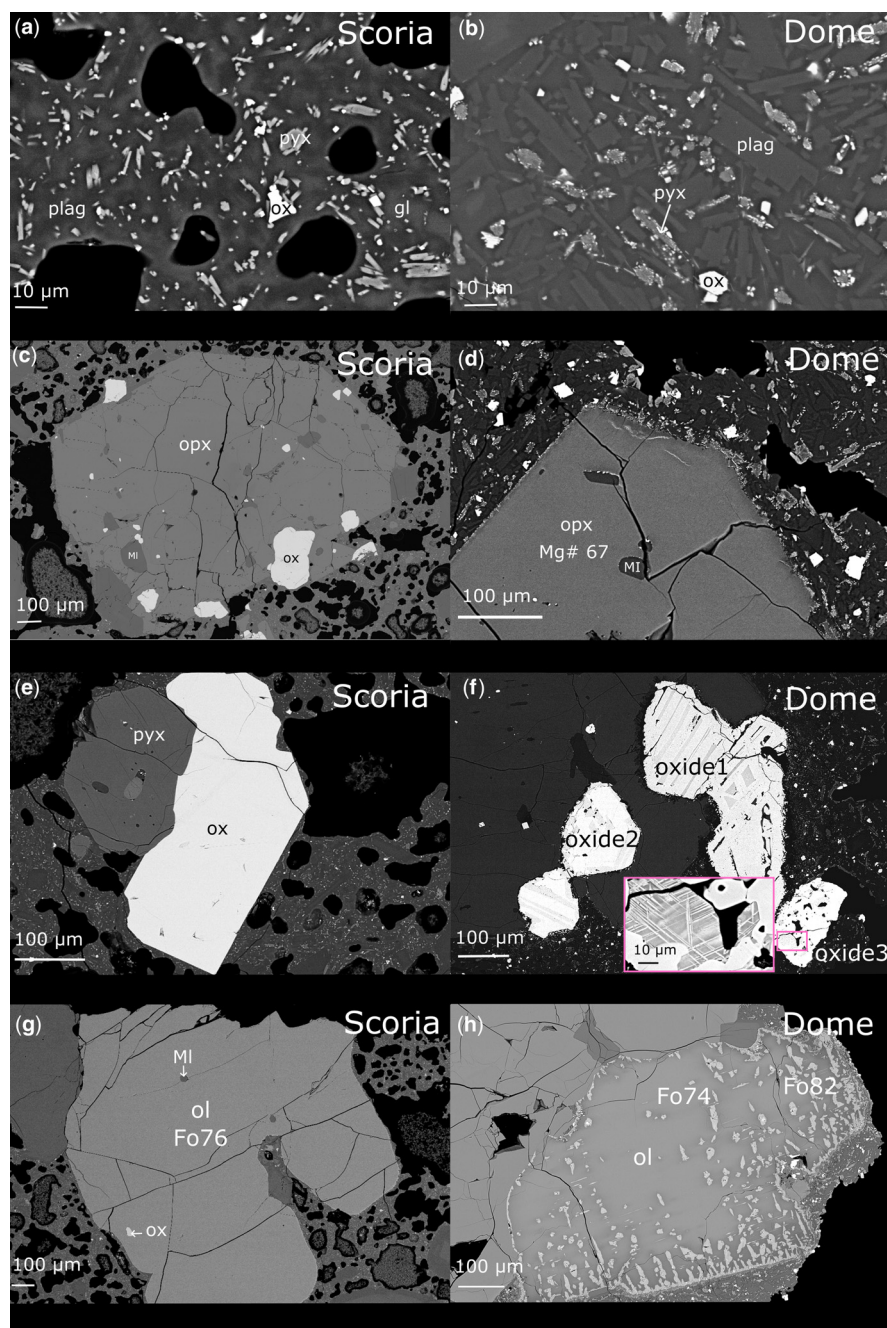
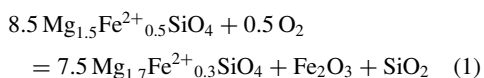


Fig. 1. Backscattered electron (BSE) images of the textural differences between the erupted dome and scoria material. (a) Glassy and vesicular scoria groundmass with skeletal microlites. (b) Microlite-rich dome groundmass containing oxide-rimmed pyroxene microlites. (c) Homogenous orthopyroxene phenocryst in scoria. (d) Orthopyroxene phenocryst in dome rimmed with oxides along grain boundaries (e) Homogenous oxide phenocryst in scoria. (f) Oxide phenocrysts in dome exhibiting different types of exsolution lamellae (oxide 1–3). Oxide 1 displays uniform trellis lamellae; oxide 2 displays irregular ‘sandwich-type’ lamellae, and oxide 3 contains cloth exsolution lamellae and recrystallized grains – see inset. (g) Homogenous olivine phenocryst in scoria. (h) Olivine phenocryst in dome exsolving Fe-oxide symplectites. Abbreviations: gl, glass; pyx, pyroxene; opx, orthopyroxene; plag, plagioclase; ox, oxide; ol, olivine; MI, melt inclusion.

magmas and can reflect different crystallization pressures, magma mixing or crustal assimilation during ascent (Barnes and Roeder 2001). In the dome, four compositionally distinct host and exsolved oxide phases are found, following the four different exsolution textures previously described (see above). Oxide 1 is an ulvöspinel-rich titanomagnetite host exsolving an Mg–Fe–Al spinel. Oxide 2 and oxide 4 are titanomagnetites exsolving titanohematite, with variable Mg, Fe, Al and Ti contents. Oxide 3 appears to be predominantly recrystallized hematite, with pockets of a dark grey (in BSE) Mg–Fe–Al spinel (pleonaste–magnesioferrite), which further exsolves a magnetite-rich phase as cloth-like lamellae (Fig. 1f inset). Oxide 3 contains no titanium except along the grain boundary previously in contact with oxide 1, suggesting diffusion of titanium between adjacent grains prior to separation.

Olivine phenocrysts. Olivine crystals in the scoria have forsterite contents of Fo65–75, separated into two distinct groups by their different manganese contents. Olivines with ~Fo65 contain *c.* 0.6 wt% MnO, whereas those with ~Fo75 contain *c.* 0.4 wt% MnO (Table 2). Mn–Mg exchange within olivine is recognized to be a function of temperature, pressure and fO_2 (Evans *et al.* 2006; Blundy *et al.* 2020) and variations in these parameters could account for the variable MnO contents. Olivine crystals in the dome range from Fo74 in the centre of the crystal, to Fo82 adjacent to symplectite exsolution at the crystal edge. The composition of the exsolved Fe-oxide phase could not be analysed directly due to the very fine grain size of the symplectites (<1 µm). The high Fo content (Fo82) and lack of orthopyroxene does, however, suggest the continuous breakdown of olivine, as described above, with hematite as the product Fe-oxide phase (Haggerty and Baker 1967; Champness 1970; Johnston and Stout 1984). Equation (1) is a balanced reaction that describes the oxidation–exsolution of olivine to form hematite symplectites in the St Vincent dome; primary olivine (Fo74; in the centre of the crystal, Fig. 1f) oxidizes to form an Mg-enriched olivine (Fo82), hematite and melt (SiO₂):



Experimental results

Experimental run conditions, phase assemblages and phase compositions for eight runs are reported in Tables 3 and 4. Microlites were analysed where sufficiently large (>2 µm). Plagioclase, orthopyroxene, and clinopyroxene phenocrysts were analysed in all runs, with olivine and Fe–Ti oxides identified in all except SV28 and SV29. Figure 2 illustrates the

experimentally-derived stability limits in T– fO_2 space of orthopyroxene phenocrysts, newly exsolved and co-existing Fe–Ti oxide phases and their textures, and the development of olivine symplectites. Plagioclase and clinopyroxene phenocrysts remain stable at all experimental conditions and are texturally and compositionally consistent in both the dome and the scoria (Table 2). Orthopyroxene phenocrysts are stable at 900°C, but progressively breakdown with increasing fO_2 at 1020°C (dashed line; Fig. 2). Host Fe–Ti oxides exsolve one or two new oxide phases at certain T– fO_2 conditions, with three co-existing oxides present at NNO + 2 in both temperature series, and above NNO + 2 at 900°C (Fig. 2). Exsolution textures also vary with temperature and fO_2 . Olivine symplectites form at and above NNO. A detailed description of the textural and compositional differences in each experiment and comparison with the dome and scoria is presented below.

Textural variations

Microlites. Microlites of plagioclase are present in all experimental runs and appear as elongate laths, with larger crystals sometimes exhibiting normal zoning (Fig. 3). The smaller microlites (<10 µm) most likely grew during experimental runs, as seen in previous reheating experiments (D’Oriano *et al.* 2013; Deardorff and Cashman 2017), whilst larger microlites (10–30 µm) exhibit new rim overgrowths and are likely remnant from the crushed scoria starting material. Pyroxene microlites are also present in all experimental runs and are acicular to subhedral in form. A small proportion of pyroxene microlites display minor alteration at NNO and 900°C (Fig. 3c); however, ubiquitous breakdown of pyroxene microlites only begins at NNO + 2 in both temperature series. The breakdown process involves pyroxene microlites becoming rimmed with oxide nanolites (Fig. 3e–h), as seen in the dome. Larger microlites in the high temperature (1020°C) series also show signs of more significant breakdown to form oxide nanolites across the entire crystal interior (Fig. 3f, h – labelled pyx). Similar pyroxene breakdown textures have been observed in oxidized juvenile ash particles (Matsumoto and Geshi 2021) and reheated crystals (D’Oriano *et al.* 2013, 2014). Oxide microlites and nanolites become more abundant in the groundmass coeval with the formation of pyroxene breakdown textures. Olivine microlites were identified in two experimental run products: SV29, at 1020°C and NNO – 2, appearing homogenous and subhedral; and SV22, at 1020°C and NNO + 2, appearing unstable with fine symplectite textures present.

Pyroxene phenocrysts. Orthopyroxene phenocrysts in experimental run products at NNO – 2 are

Table 4. Average chemical analyses of experimental run products

	<i>n</i>	SiO ₂	TiO ₂	Al ₂ O ₃	FeO ^T	MnO	MgO	CaO	Na ₂ O	K ₂ O	P ₂ O ₅	Total
Run#	SV31, AIR, 1020°C											
plag												
phenocryst core	30	45.43	0.01	34.10	0.64	0.01	0.05	18.12	1.27	0.02	0.02	99.70
sd		1.62	0.01	1.09	0.06	0.01	0.01	1.25	0.69	0.02	0.02	
phenocryst rim	7	52.46	0.04	29.42	0.64	0.01	0.08	12.71	4.25	0.08	0.01	99.72
sd		0.40	0.01	0.28	0.04	0.01	0.01	0.33	0.15	0.01	0.01	
microlite	7	54.68	0.08	28.23	1.13	0.02	0.14	11.54	4.39	0.21	0.04	100.49
sd		6.01	0.05	4.05	0.38	0.02	0.11	4.02	1.84	0.18	0.02	
opx												
phenocryst	12	55.27	0.23	0.67	15.06	0.76	26.78	1.61	0.02	0.01	0.01	100.42
sd		1.78	0.02	0.14	3.07	0.07	2.58	0.33	0.02	0.01	0.01	0.92
cpx												
phenocryst	28	51.42	0.54	1.94	9.97	0.40	14.41	20.36	0.28	bd	0.02	99.36
sd		0.83	0.14	0.62	0.39	0.03	0.35	0.30	0.02		0.01	
microlite	2	53.06	0.55	3.51	5.87	0.58	16.15	19.87	0.84	0.11	0.05	100.62
sd		0.74	0.11	0.14	0.73	0.01	0.01	0.29	0.12	0.01	0.01	
ol												
host phenocryst	5	42.39	0.00	0.01	2.88	0.36	54.74	0.10	0.01	bd	0.01	100.49
sd		0.18	0.00	0.01	1.51	0.04	1.84	0.01	0.01		0.02	
symplectite mixed analysis	4	39.71	0.01	0.10	28.21	0.42	30.67	0.26	0.02	bd	0.01	99.46
sd		2.42	0.01	0.14	6.36	0.13	3.38	0.12	0.01		0.01	
oxide rim – mgf	6	0.42	0.01	1.53	71.47	0.95	16.14	0.03	0.01	bd	0.01	90.68
sd		0.67	0.01	0.15	0.62	0.03	0.59	0.01	0.01		0.01	
oxide rim – hm	4	0.10	0.57	0.48	86.77	0.23	0.47	0.03	bd	bd	bd	88.68
sd		0.03	0.21	0.10	0.50	0.02	0.17	0.02				
oxide												
tmt host	3	0.05	9.61	1.53	75.08	0.62	3.59	0.03	0.01	bd	bd	90.58
sd		0.03	0.65	1.00	0.58	0.01	1.36	0.02	0.02			
exsolved tht	3	0.18	33.32	1.97	52.40	0.24	2.10	0.04	bd	bd	bd	90.37
sd		0.09	0.58	1.35	0.62	0.14	0.20	0.01				
Run#	SV27, AIR, 900°C											
plag												
phenocryst core	24	47.26	0.03	33.01	0.71	0.01	0.05	16.73	1.96	0.03	0.02	99.84
sd		2.01	0.01	1.27	0.09	0.02	0.02	1.52	0.76	0.02	0.01	
phenocryst rim	30	52.50	0.04	29.80	0.65	0.01	0.07	12.74	3.82	0.07	0.02	99.74
sd		1.48	0.01	0.67	0.05	0.02	0.01	0.96	0.39	0.02	0.01	
microlite	3	58.80	0.22	23.11	1.74	0.03	0.47	8.10	5.26	0.31	0.09	98.13
sd		4.98	0.15	3.19	0.25	0.04	0.24	2.17	0.82	0.17	0.06	
opx												
phenocryst	10	52.79	0.28	0.96	20.26	0.65	23.58	1.73	0.02	bd	bd	100.27
sd		0.31	0.07	0.32	0.60	0.07	0.49	0.19	0.02			
cpx												
phenocryst	6	51.35	0.48	1.70	10.70	0.51	14.48	20.03	0.42	0.01	0.03	99.7529
sd		1.71	0.39	1.51	1.89	0.11	0.66	1.35	0.22	0.02	0.02	
ol												
host phenocryst	4	41.10	0.02	0.01	5.99	0.43	53.23	0.15	0.01	0.00	0.02	101.00
sd		0.25	0.01	0.01	0.66	0.03	1.02	0.01	0.02	0.01	0.00	
symplectite mixed analysis	4	39.30	0.04	0.07	28.09	0.43	30.36	0.30	0.03	0.01	0.03	98.69
sd		1.63	0.02	0.02	4.42	0.02	3.74	0.13	0.01	0.00	0.01	
oxide												
tmt host 1	5	0.20	15.90	1.87	72.02	0.33	2.01	0.01	bd	bd	bd	92.46
sd		0.16	1.72	0.17	1.14	0.02	0.09	0.01				
exsolved 1 spn	5	0.09	1.71	9.74	76.04	1.36	5.79	0.00	0.02	bd	bd	94.88
sd		0.01	0.25	0.88	1.13	0.06	0.34	0.01	0.03			
tmt host 2	5	0.10	7.06	2.66	77.89	0.34	1.51	0.05	0.01	bd	0.01	89.93
sd		0.01	1.86	0.48	1.67	0.10	0.30	0.02	0.01		0.00	

(Continued)

Table 4. *Continued.*

	<i>n</i>	SiO ₂	TiO ₂	Al ₂ O ₃	FeO ^T	MnO	MgO	CaO	Na ₂ O	K ₂ O	P ₂ O ₅	Total
exsolved 2 spn	4	0.09	1.75	14.97	63.94	2.15	10.70	0.05	0.01	bd	0.01	94.09
sd		0.01	1.18	1.91	2.98	0.26	0.69	0.02	0.01		0.01	
exsolved 2 tht	3	0.20	37.31	2.61	48.57	0.25	2.24	0.07	0.01	bd	0.01	91.50
sd		0.09	5.83	0.13	6.00	0.06	0.66	0.04	0.01		0.01	
Run#	SV22, NNO + 2, 1020°C											
plag												
phenocryst core	7	44.98	0.02	34.17	0.78	0.01	0.09	18.36	0.90	0.03	0.02	99.37
sd		0.84	0.03	0.71	0.13	0.03	0.09	0.38	0.11	0.04	0.01	
phenocryst rim	5	51.71	0.05	29.96	0.95	0.03	0.09	13.36	3.84	0.10	0.02	100.10
sd		2.78	0.02	1.55	0.08	0.01	0.02	1.97	0.90	0.04	0.01	
microlite core	1	52.43	0.08	29.17	1.05	0.03	0.15	13.10	3.51	0.22	0.03	99.77
opx												
phenocryst	1	53.05	0.33	1.30	16.98	0.82	26.04	1.82	0.03	bd	0.01	100.37
microlite	1	55.40	0.40	1.11	8.86	1.15	29.94	2.59	0.10	0.03	0.03	99.60
cpx												
phenocryst	3	52.80	0.69	3.23	9.28	0.71	15.93	16.37	0.67	0.14	0.06	99.87
sd		0.82	0.14	0.90	0.37	0.20	0.97	3.16	0.16	0.15	0.04	
ol												
host phenocryst	4	41.77	bd	0.01	7.66	0.43	51.13	0.09	0.01	0.01	0.01	101.13
sd		0.21		0.01	0.24	0.02	0.52	0.00	0.00	0.01	0.01	
symplectite mixed	3	35.18	0.03	0.14	39.17	0.47	24.67	0.42	0.02	bd	bd	100.13
analysis												
sd		4.83	0.01	0.13	9.71	0.02	3.34	0.23	0.01			
oxide rim – mgf	2	0.31	0.10	0.62	81.29	0.54	8.75	0.04	0.01	0.07	bd	91.77
sd		0.31	0.04	0.60	0.68	0.02	0.30	0.01	0.03	0.08		
oxide												
tmt host	3	0.08	14.46	2.21	71.29	0.42	2.70	0.03	bd	bd	bd	91.33
sd		0.02	1.05	0.27	0.69	0.07	0.22	0.03				
exsolved spn	3	0.10	2.15	6.61	75.25	1.43	7.45	0.06	bd	bd	bd	93.19
sd		0.01	0.14	0.11	0.20	0.02	0.35	0.00				
exsolved tht	4	0.11	35.96	3.03	48.87	0.26	2.64	0.16	bd	bd	bd	91.17
sd		0.01	1.74	0.10	1.56	0.02	0.07	0.01				
Run#	SV33, NNO + 2, 900°C											
plag												
phenocryst core	10	46.58	0.02	32.52	0.66	0.02	0.04	16.17	2.02	0.03	0.02	98.10
sd		1.58	0.01	0.91	0.07	0.01	0.01	0.87	0.17	0.01	0.01	
phenocryst rim	11	51.95	0.05	29.71	0.78	0.01	0.07	13.02	4.10	0.08	0.03	99.82
sd		0.46	0.04	0.36	0.25	0.01	0.01	0.35	0.16	0.03	0.01	
microlite	5	58.51	0.17	24.70	1.52	0.03	0.10	8.23	5.81	0.53	0.07	99.68
sd		2.55	0.10	1.83	0.39	0.01	0.03	1.49	0.42	0.26	0.03	
opx												
phenocryst	11	53.28	0.35	1.16	18.38	0.59	24.45	1.71	0.03	bd	bd	100.00
sd		0.30	0.03	0.10	0.57	0.08	0.59	0.07	0.01			
microlite	10	53.64	0.63	2.91	16.65	1.00	18.46	6.39	0.44	0.23	0.07	100.45
sd		3.09	0.20	2.36	3.64	0.17	3.61	3.44	0.37	0.29	0.06	
cpx												
phenocryst	15	51.08	0.51	4.46	9.49	0.40	13.62	19.24	0.58	0.01	0.02	99.42
sd		0.51	0.16	6.70	2.39	0.10	3.68	1.48	0.87	0.03	0.01	
ol												
host phenocryst	13	39.76	0.01	0.00	13.52	0.61	45.99	0.12	bd	bd	0.01	100.03
sd		0.63	0.01	0.01	2.47	0.18	1.73	0.04			0.01	
symplectite mixed	5	37.93	0.03	0.13	35.44	0.59	24.20	0.31	0.02	bd	0.01	98.68
analysis												
sd		0.36	0.03	0.16	1.27	0.18	0.48	0.15	0.01		0.01	
oxide rim – hm	3	0.71	2.76	0.91	80.55	0.62	5.14	0.14	0.01	0.02	bd	90.95
sd		0.42	2.51	0.47	1.86	0.19	0.53	0.04	0.01	0.01		
oxide												
tmt host	8	0.49	15.30	2.25	70.56	0.39	2.23	0.11	0.02	0.01	0.01	91.53

(Continued)

Table 4. *Continued.*

	<i>n</i>	SiO ₂	TiO ₂	Al ₂ O ₃	FeO ^T	MnO	MgO	CaO	Na ₂ O	K ₂ O	P ₂ O ₅	Total
sd		0.50	2.83	0.88	1.49	0.12	0.35	0.08	0.06	0.01	0.01	
exsolved spn	3	0.72	3.35	6.39	78.12	0.98	4.49	0.08	0.03	0.01	0.01	94.34
sd		0.65	0.22	0.29	0.40	0.05	0.05	0.01	0.04	0.02	0.01	
exsolved tht	2	0.42	43.04	2.51	41.90	0.19	3.04	0.42	0.27	0.12	0.01	92.02
sd		0.03	1.88	0.15	0.03	0.03	0.17	0.29	0.26	0.10	0.00	
Run#	SV25, NNO, 1020°C											
plag												
phenocryst core	1	46.31	0.04	33.11	0.91	0.00	0.07	15.72	1.69	0.03	0.01	97.90
phenocryst rim	1	56.07	0.09	26.52	1.16	0.04	0.13	9.33	4.96	0.23	0.03	98.55
microlite	2	64.99	0.81	17.22	3.31	0.14	0.92	5.16	3.51	1.23	0.30	97.61
sd		2.73	0.29	3.42	0.89	0.05	0.35	1.57	1.10	0.39	0.13	
opx												
phenocryst core	2	52.85	0.32	0.98	17.91	0.59	24.72	1.58	0.03	bd	bd	99.00
sd		1.09	0.03	0.06	0.98	0.04	1.24	0.10	0.03			
phenocryst rim	1	54.60	0.30	0.83	14.42	0.67	27.94	1.72	0.04	0.00	0.02	100.54
exsolved oxide	1	bd	0.14	0.02	81.97	0.56	9.04	0.03	bd	0.14	bd	91.91
cpx												
phenocryst	1	52.01	0.67	2.64	10.72	0.86	18.98	11.35	0.43	0.07	0.04	97.76
ol												
host phenocryst	2	38.76	0.02	0.00	15.72	0.73	43.98	0.12	0.02	0.01	bd	99.41
sd		0.10	0.01	0.00	0.02	0.02	0.10	0.00	0.02	0.01		
symplectite mixed	2	30.37	1.20	1.10	43.11	0.75	18.92	0.71	0.04	0.01	0.03	96.26
analysis												
sd		7.23	0.36	0.25	9.70	0.06	4.07	0.20	0.03	0.01	0.01	
oxide												
tmt host	2	0.30	5.49	2.75	76.79	0.89	5.63	0.06	bd	bd	bd	92.06
sd		0.01	0.58	0.05	0.01	0.01	0.04	0.02				
exsolved tmt	2	0.25	20.72	0.88	65.42	0.38	3.19	0.06	0.03	bd	0.01	91.09
sd		0.03	0.05	0.02	0.19	0.01	0.01	0.04	0.01		0.01	
Run#	SV32, NNO, 900°C											
plag												
phenocryst core	1	45.03	0.00	35.04	0.68	0.02	0.05	18.82	0.74	0.01	0.02	100.45
phenocryst rim	10	53.55	0.03	28.87	0.57	0.01	0.08	12.07	4.58	0.09	0.02	99.89
sd		0.57	0.01	0.37	0.03	0.01	0.01	0.39	0.23	0.01	0.01	
microlite	1	58.31	0.20	24.95	1.51	0.03	0.20	9.05	5.43	0.47	0.10	100.27
opx												
phenocryst	10	53.21	0.33	1.19	18.65	0.64	23.50	1.68	0.04	0.01	bd	99.27
sd		0.49	0.04	0.13	1.36	0.05	1.13	0.06	0.01	0.01		
cpx												
phenocryst	20	51.31	0.59	2.11	10.60	0.43	14.55	19.77	0.27	0.00	0.02	99.69
sd		0.25	0.03	0.09	0.12	0.03	0.12	0.17	0.02	0.01	0.01	
microlite	3	52.28	0.86	4.38	17.85	0.74	14.48	7.39	0.65	0.39	0.16	99.19
sd		2.13	0.17	0.59	0.20	0.07	2.36	1.34	0.41	0.23	0.03	
ol												
host phenocryst	5	44.10	0.01	0.00	3.76	0.33	52.59	0.14	0.01	bd	0.01	100.95
sd		2.82	0.01	0.00	0.20	0.04	1.49	0.01	0.01		0.01	
symplectite mixed	4	45.05	0.01	0.06	27.26	0.40	26.60	0.18	0.01	bd	bd	99.58
analysis												
sd		4.54	0.01	0.00	2.78	0.03	1.74	0.02	0.00			
oxide												
tmt host	2	0.48	11.80	1.97	72.22	0.18	1.41	0.21	0.02	0.02	bd	88.43
sd		0.11	0.14	0.29	1.06	0.02	0.26	0.02	0.01	0.01		
exsolved tht	3	0.42	36.42	2.60	49.62	0.14	1.36	0.14	bd	0.02	bd	90.82
sd		0.02	2.36	0.06	2.07	0.08	1.01	0.02		0.00		
Run#	SV29, NNO – 2, 1020°C											
plag												
phenocryst core	8	45.72	0.01	33.37	0.61	0.02	0.05	17.74	1.38	0.03	0.02	98.99
sd		1.40	0.01	1.06	0.01	0.03	0.02	1.19	0.70	0.02	0.02	

(Continued)

Table 4. *Continued.*

	<i>n</i>	SiO ₂	TiO ₂	Al ₂ O ₃	FeO ^T	MnO	MgO	CaO	Na ₂ O	K ₂ O	P ₂ O ₅	Total
phenocryst rim	9	51.39	0.03	29.67	0.67	0.01	0.07	13.43	3.84	0.07	0.02	99.24
sd		2.21	0.01	1.31	0.07	0.02	0.01	1.59	0.92	0.03	0.01	
microlite core	3	46.62	0.02	32.55	0.77	0.00	0.08	16.64	2.03	0.05	0.02	98.81
sd		0.13	0.01	0.07	0.06	0.03	0.03	0.07	0.01	0.01	0.03	
microlite rim	4	54.30	0.07	27.39	0.80	0.01	0.15	10.86	5.18	0.17	0.03	98.99
sd		0.73	0.01	0.66	0.12	0.02	0.03	0.52	0.18	0.01	0.03	
opx												
phenocryst core	1	52.71	0.31	0.97	20.06	0.71	23.66	1.59	0.05	bd	bd	100.08
sd												
phenocryst rim	3	52.22	0.36	0.75	21.38	0.74	18.70	5.63	0.08	0.01	bd	99.92
sd		0.29	0.06	0.13	0.39	0.10	0.44	1.00	0.01	0.01		
microlite	3	51.85	0.40	1.33	20.38	0.71	20.57	4.01	0.10	0.02	0.02	99.41
sd		0.51	0.04	0.31	0.49	0.05	1.17	0.51	0.09	0.02	0.01	
cpx												
phenocryst core	9	51.98	0.50	1.87	10.56	0.42	14.23	19.83	0.33	0.02	0.03	99.82
sd		0.40	0.11	0.70	0.31	0.04	0.42	0.64	0.12	0.04	0.02	
phenocryst rim	3	52.03	0.43	1.46	10.58	0.40	14.18	20.32	0.30	0.00	0.02	99.77
sd		0.07	0.02	0.07	0.09	0.02	0.02	0.07	0.01	0.01	0.04	
ol												
host phenocryst	2	35.95	0.03	0.01	37.19	0.75	26.26	0.40	bd	bd	0.01	100.65
sd		0.42	0.00	0.04	0.23	0.06	0.06	0.00			0.01	
microlite	1	35.77	0.05	0.01	33.55	0.67	29.91	0.38	0.04	0.01	0.04	100.45
sd												
Run#		SV28, NNO – 2, 900°C										
plag												
phenocryst core	4	49.34	0.03	30.82	0.68	0.02	0.07	14.99	2.96	0.05	0.02	99.00
sd		2.96	0.02	2.20	0.08	0.03	0.02	2.33	1.31	0.03	0.02	
phenocryst rim	16	52.92	0.04	28.66	0.66	0.00	0.07	12.19	4.49	0.08	0.02	99.17
sd		0.66	0.01	0.48	0.07	0.02	0.02	0.45	0.21	0.01	0.02	
microlite core	2	47.61	0.04	31.01	0.82	0.03	0.08	15.74	2.64	0.05	0.01	98.05
sd		0.90	0.01	0.82	0.00	0.04	0.01	0.74	0.57	0.01	0.02	
microlite rim	7	56.09	0.12	25.62	1.13	0.04	0.15	9.52	5.68	0.25	0.05	98.68
sd		2.03	0.07	2.11	0.34	0.02	0.06	1.54	0.50	0.13	0.02	
opx												
microlite	6	52.00	0.69	3.11	18.10	0.79	15.51	8.43	0.46	0.20	0.08	99.39
sd		1.19	0.13	0.44	2.51	0.08	2.09	2.67	0.22	0.12	0.04	
cpx												
phenocryst	4	50.92	0.59	2.30	10.17	0.40	14.49	20.00	0.29	0.01	0.03	99.27
sd		1.15	0.15	0.86	0.68	0.09	0.25	0.33	0.05	0.02	0.03	
microlite	1	49.47	1.00	3.37	12.44	0.48	14.33	17.15	0.35	0.02	0.06	98.69
oxide												
tmt host	1	0.19	14.42	3.49	70.18	0.72	1.32	0.17	bd	0.02	bd	90.76
exsolved tht	1	4.53	29.09	0.93	59.01	0.44	1.18	0.27	0.31	0.08	bd	95.90

Abbreviations as in Table 2, as well as: hm, hematite; mgf, magnesioferrite; sd, standard deviation.

All Fe measured as FeO (FeO^T)

n is number of analyses of each phase reported

homogenous, with those at 900°C appearing stable, whilst those at 1020°C showing signs of resorption (Fig. 4a, b). At and above NNO, and in the low temperature (900°C) series, oxide nanolites form along grain boundaries and within fractures of orthopyroxene phenocrysts (Fig. 4c, e, g), similar to those seen in the dome. The breakdown of orthopyroxene phenocrysts is much more prominent in the higher temperature series, at and above NNO. Oxide nanolites form across the crystal

interior, becoming more extensive and abundant with an increase in *f*O₂ (Fig. 4d, f, h), and no longer restricted to crystal edges or along fractures. Such textures define the stability limit of orthopyroxene with respect to temperature and oxygen fugacity, and delineate where orthopyroxene becomes a metastable phase at one atmosphere (Fig. 2). Clinopyroxene phenocrysts appear euhedral and stable in all runs, with no sign of any overgrowth or resorption.

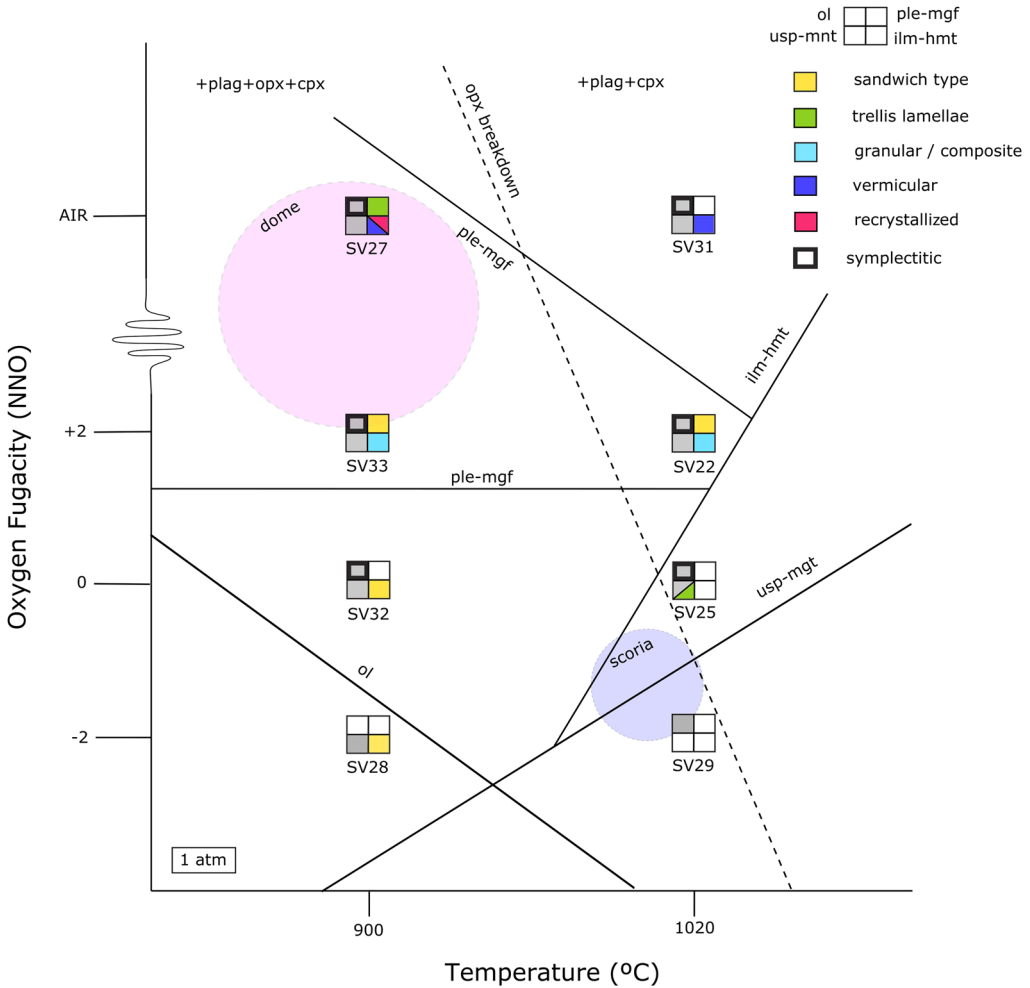


Fig. 2. Experimental phase diagram illustrating stability of iron–titanium oxide exsolution phases and textures, olivine symplectites and orthopyroxene in T – fO_2 space at one atmosphere. Grey shading illustrates phases present, with different colours representing the type of exsolution observed. Exsolution descriptions after Haggerty (1976a). Bold outline indicates the presence of symplectite exsolution in olivine. Dashed line depicts breakdown of orthopyroxene. Pink and blue shaded areas represent proposed T – fO_2 conditions for the dome and scoria upon eruption. Abbreviations as in Figure 1 as well as usp, ulvöspinel; mnt, magnetite; ilm, ilmenite; hmt, hematite; ple, pleonaste; mgf, magnesioferrite.

Iron–titanium oxide phenocrysts. At the most reduced ($NNO - 2$) experimental conditions, Fe–Ti oxides are absent at 1020°C; at 900°C they are identified only as microlites, with some crystals displaying regions of weak exsolution. In experiments at NNO , irregular ‘sandwich-type’ exsolution is observed at 900°C (Fig. 5a), and weak trellis exsolution lamellae form along two planes at 1020°C (Fig. 5b). At $NNO + 2$, two different phases exsolve along the edge of Fe–Ti crystals in both temperature series, each with a slightly different form. The first exsolution phase forms small irregular granules at the crystal edge that appear

darkest (low- Z) in BSE images. The second exsolution phase, more dominant at 1020°C, forms subtle ‘sandwich-type’ lamellae along the grain boundary, appearing as a lighter grey (high- Z) in BSE images (Fig. 5c, d). The exsolution of phases along grain boundaries and fractures supports oxidation–exsolution by an external oxidizing agent (Haggerty 1976a, 1991). Dome oxide 2 and oxide 4 exhibit well-developed sandwich-type lamellae, suggesting conditions in the dome were likely above $NNO + 2$ as sandwich-type lamellae become better developed with increasing fO_2 (Buddington and Lindsley 1964).

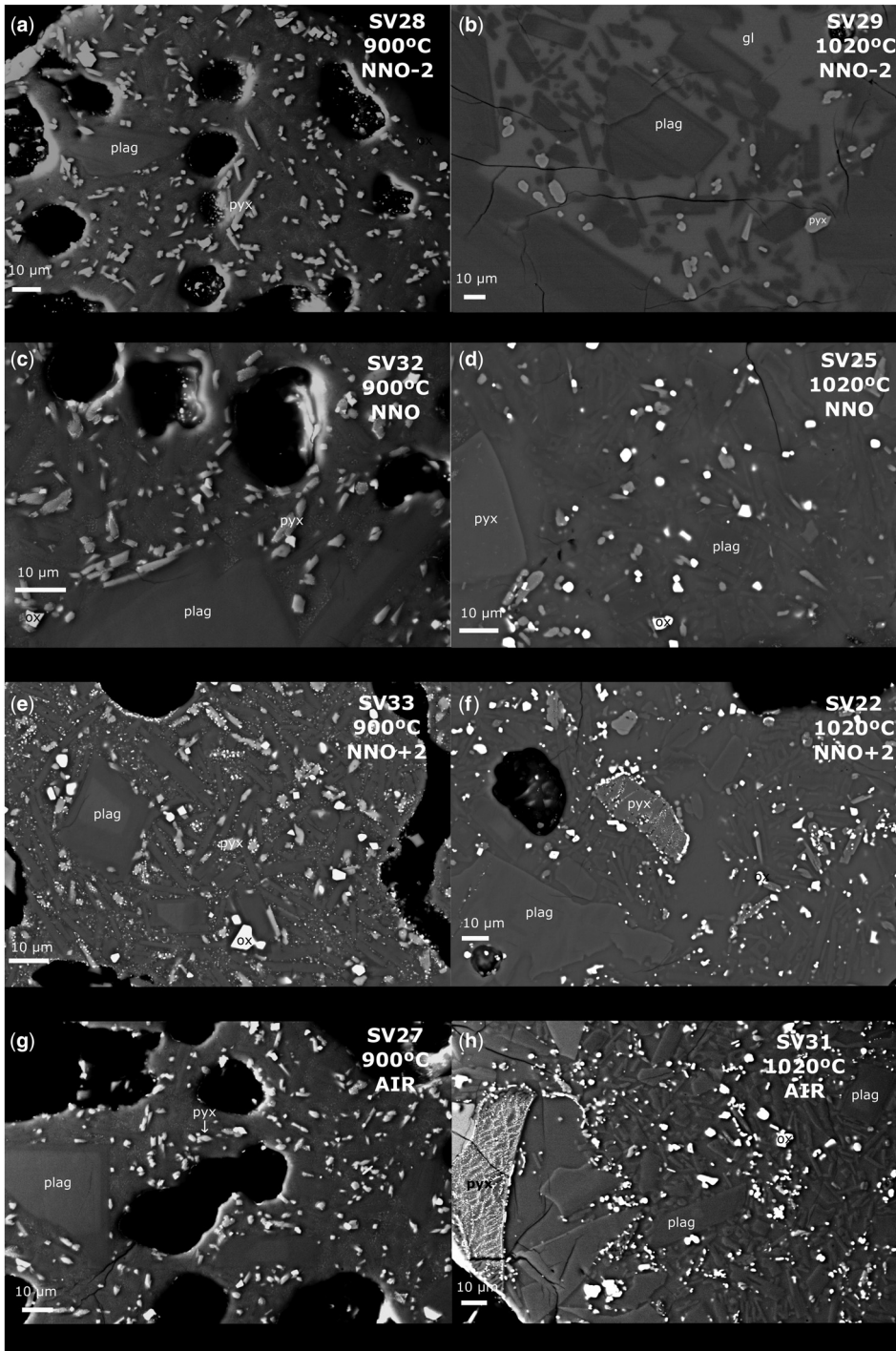


Fig. 3. BSE images of the microlite-rich groundmass in experimental run products. Pyroxene microlites are stable below NNO (a–d) but begin to form oxides along their rims at oxygen fugacities \geq NNO + 2; co-eval with an increase in the abundance of oxide microlites (e–h). No oxide microlites are present in SV29 (b). Abbreviations as in Figure 1.

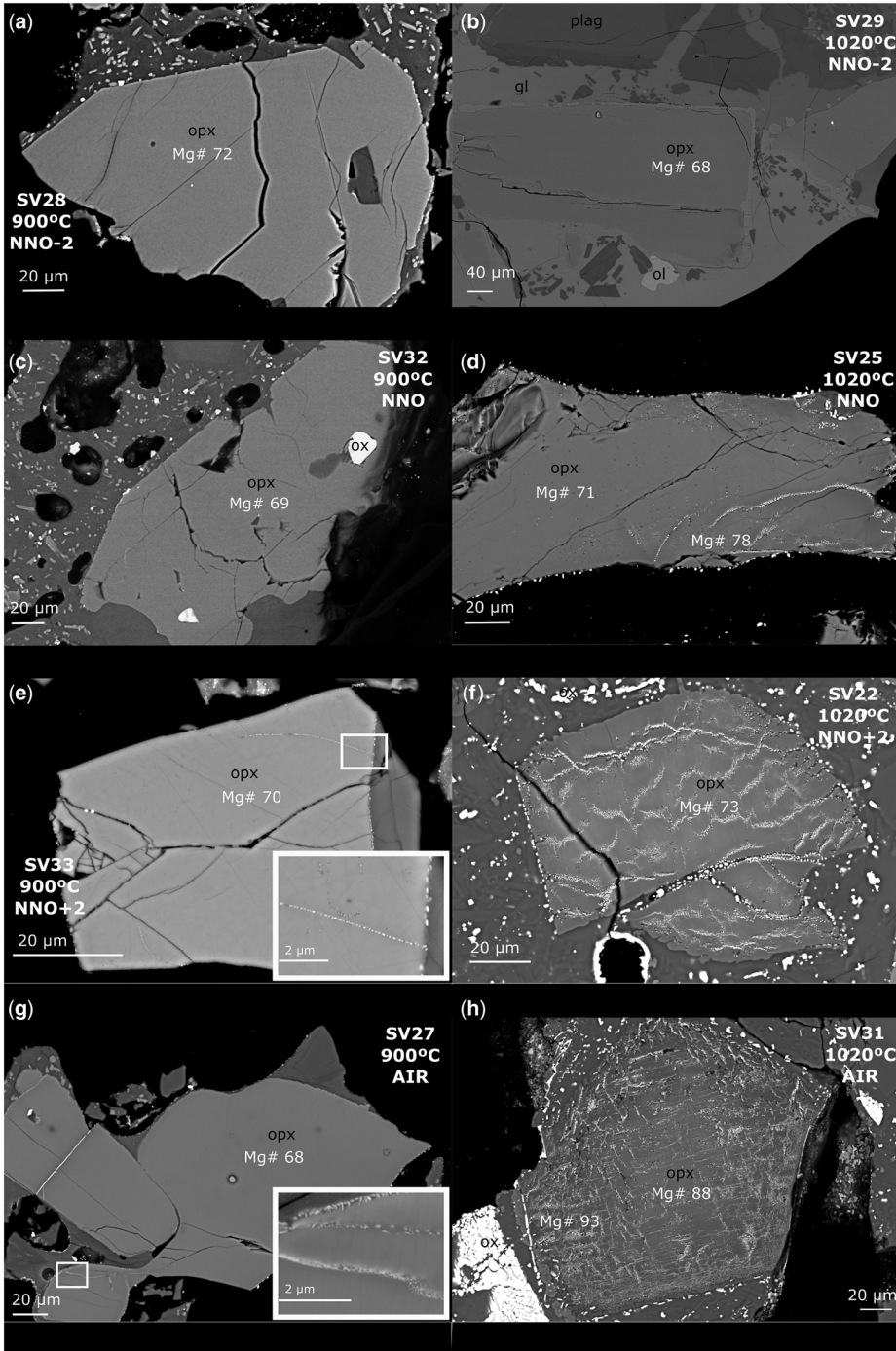


Fig. 4. BSE images of the breakdown textures observed in orthopyroxene phenocrysts in experimental run products. Orthopyroxene phenocrysts are homogenous at the most reduced experimental conditions (a, b) and at NNO at 900°C (c). At \geq NNO + 2 and 900°C, orthopyroxenes begin to be rimmed with oxides (e, g). At \geq NNO and 1020°C, orthopyroxenes undergo significant alteration, breaking down to form oxide nanolites across the crystal interior (d, f, h). Mg# in moles calculated as $\text{Mg}/(\text{Mg} + \text{Fe})$, assuming all Fe as Fe^{2+} . Abbreviations as in Figure 1.

Experiments run in air produced significantly altered Fe–Ti oxides. In experiment SV27 at 900°C two Fe–Ti oxide crystals were identified, each with different exsolution textures and compositions. The

first oxide (SV27 oxide 1, not shown) displays coarse well-developed trellis lamellae along two planes, similar to dome oxide 1. The second oxide (SV27 oxide 2; Fig. 5e) exsolves two phases, one

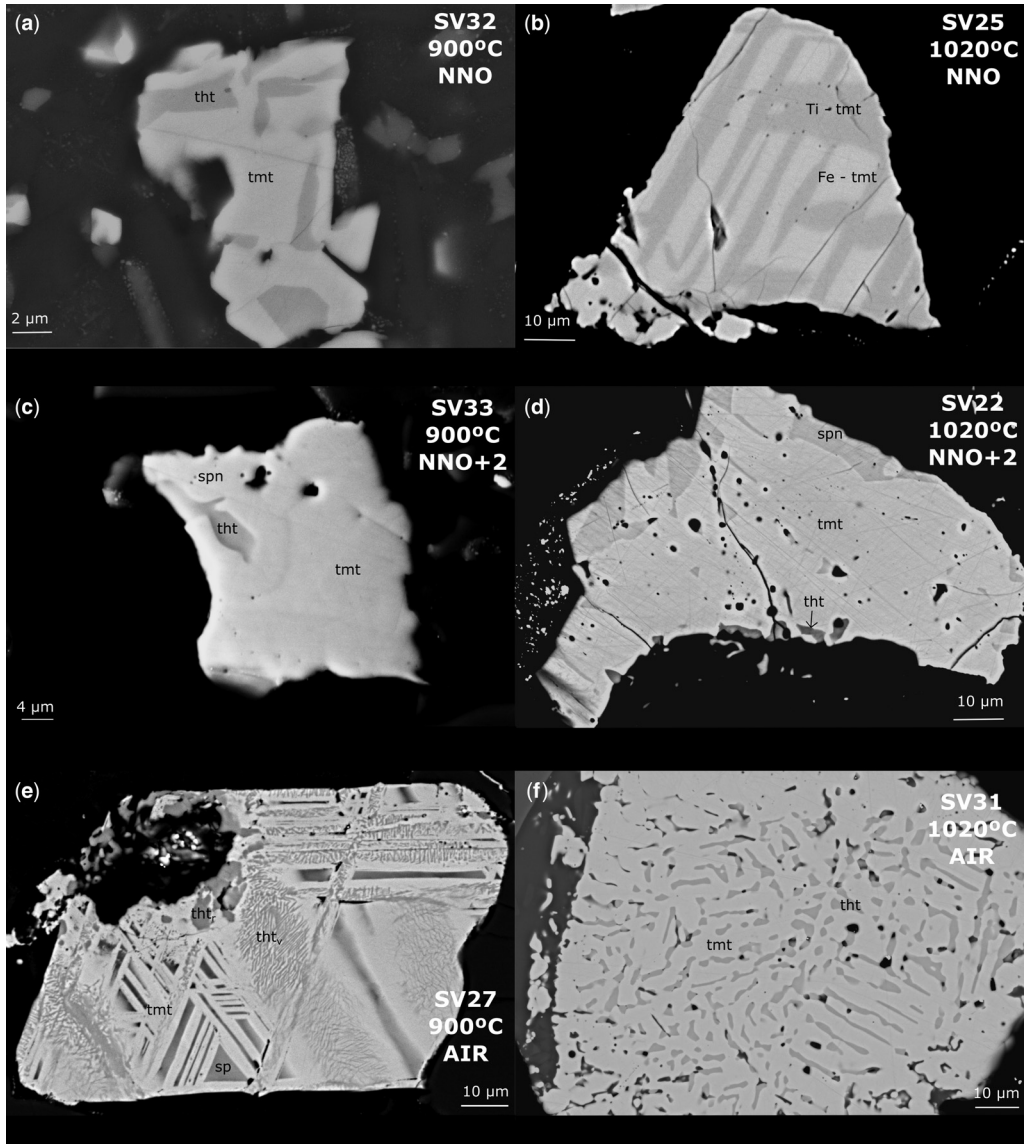


Fig. 5. BSE images of exsolved oxide microlites and phenocrysts in experimental run products. (a) Host titanomagnetite microlite (tmt) exsolving irregular blebs of titanohematite (tht). (b) Iron-rich titanomagnetite host exsolving trellis lamellae of titanium enriched titanomagnetite. (c) Titanomagnetite host exsolving titanohematite and Mg–Fe–Al spinel (spn) at the edge of the crystal. (d) Co-eval exsolution of titanohematite as composite blebs and Mg–Fe–Al spinel as irregular sandwich-type lamellae, both at the edge of the crystal. (e) Titanomagnetite host with well-developed coarse trellis lamellae of Mg–Fe–Al spinel along three planes and patches of vermicular titanohematite exsolution (tht_v) and some recrystallized grains of titanohematite (tht_r). (f) Titanomagnetite host with ubiquitous vermicular exsolution of titanohematite.

as coarse trellis lamellae along three planes, and the other as weak vermicular exsolution and as recrystallized granules. Recrystallization is also observed in dome oxide 3. At 1020°C Fe–Ti oxides undergo extreme vermicular exsolution, with grains appearing anhedral and unstable (Fig. 5f). Only the exsolution textures observed in the air experiment at 900°C appear similar to those in the dome. Figure 2 summarizes the range of Fe–Ti oxide exsolution textures observed in all experimental run products and highlights the change from ‘sandwich-type’ exsolution to granular and trellis lamellae, to vermicular and finally recrystallization textures with increasing fO_2 .

Olivine phenocrysts. At NNO – 2, olivine is not present in the low temperature series. New subhedral microlites were observed in the high temperature series (Fig. 4b), but no phenocrysts. Olivine phenocrysts are present in all experiments at and above NNO and display symplectite exsolution textures, as shown in Figure 6. At NNO and 900°C, linear symplectite bands traverse the crystal, with very fine exsolution stemming from the centre of bands. A small oxide diffusion rim is also present along the top edge of the olivine crystal (Fig. 6a). At NNO and 1020°C, the symplectitic olivine is hosted in an orthopyroxene grain, with exsolution extending inwards from the grain boundary (Fig. 6b). Increasing fO_2 results in more prominent exsolution and oxide diffusion rims. At NNO + 2 and 900°C, coarse symplectitic bands form, with well-developed fibrous exsolution lobes (‘budding’ after Haggerty and Baker 1967) growing from the centre of bands (Fig. 6c). At NNO + 2 and 1020°C, symplectite exsolution occurs in the form of clusters, with occasional thin exsolution bands or rods stretching between (Fig. 6d). Olivines exposed to air at 900°C illustrate well-developed fibrous symplectite lobes along the edge of the crystal and stemming from a single central band (Fig. 6e). In air and at 1020°C, symplectite exsolution is ubiquitous across the entire crystal and forms clusters of elongated symplectites connected by thin rods (Fig. 6f), similar to olivines observed in high temperature oxidized scoria samples (Ejima *et al.* 2017) and in lunar samples (Bell *et al.* 1975).

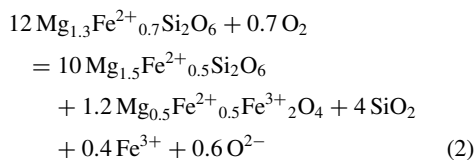
Compositional variations

Microlites. Experimental unzoned plagioclase microlites have anorthite contents ranging from An₄₄ to An₅₃, whilst limited analyses of zoned plagioclase microlites found core values of An_{75–82} and a singular rim value of An₅₆ (Table 3). Figure 7 illustrates the variation in An contents of unzoned and zoned plagioclase microlites in experimental runs and in the natural dome and scoria samples. Experimental plagioclase An contents are lower

than the U3 scoria starting material in all runs, supporting growth of new (lower An) microlites and rims during experimental runs. Although only few analyses of pyroxene microlites were obtained, those grown at more reduced experimental conditions have lower Mg numbers (Mg# 59–64 opx; Mg# 67 cpx) compared to those in more oxidizing conditions with higher Mg numbers (Mg# 61–86 opx; Mg# 75–83 cpx; Table 3), consistent with the changing proportions of Fe²⁺ and Fe³⁺ in the system. Pyroxene microlite Mg# values in the dome and scoria are more similar to experimental runs at more oxidizing conditions, suggesting crystallization at or above NNO + 2 (Fig. 7). Additionally, pyroxene microlites rimmed with Fe-oxides become depleted in Fe²⁺ thus enriched in Mg²⁺, giving them higher Mg# values.

Pyroxene phenocrysts. The composition of orthopyroxene phenocrysts varies depending on the amount of alteration experienced and volume of breakdown Fe-oxides formed. In the low temperature experimental series, Mg numbers of host orthopyroxene phenocrysts show little variation, from Mg# 68–70. In the higher temperature series, orthopyroxene crystals experience more significant breakdown, forming an abundance of Fe-oxide nanolites. Formation of Fe-oxides depletes the host orthopyroxene in Fe²⁺, thus increasing its Mg number. Mg numbers increase from core to rim and with increasing fO_2 , for example Mg# 71–78 at the NNO buffer and Mg# 88–93 in air. This supports a decrease in orthopyroxene stability with increasing oxidation state at 1020°C (Fig. 2). Clinopyroxene phenocrysts remain stable, with Mg numbers ranging from Mg# 71–76 (Table 3). This may reflect the greater ability of clinopyroxene to incorporate Fe³⁺ relative to orthopyroxene.

Only one successful analysis of an oxide nanolite within an orthopyroxene crystal is reported. Its composition is magnesioferrite (SV25; Table 4) with considerable Fe³⁺, thus supporting oxidation–exsolution. Equation (2) is a balanced reaction that describes the oxidation of an original magmatic orthopyroxene (Mg# 71) to form an Mg-enriched orthopyroxene rim (Mg# 78) and magnesioferrite. SiO₂, Fe³⁺ and O^{2–}, required to balance the reaction, are assumed to be present in the melt. The initial low-Mg orthopyroxene composition was obtained from the centre of the phenocryst (Fig. 4d). Negligible change is observed in other cation species such as Ca and Mn.



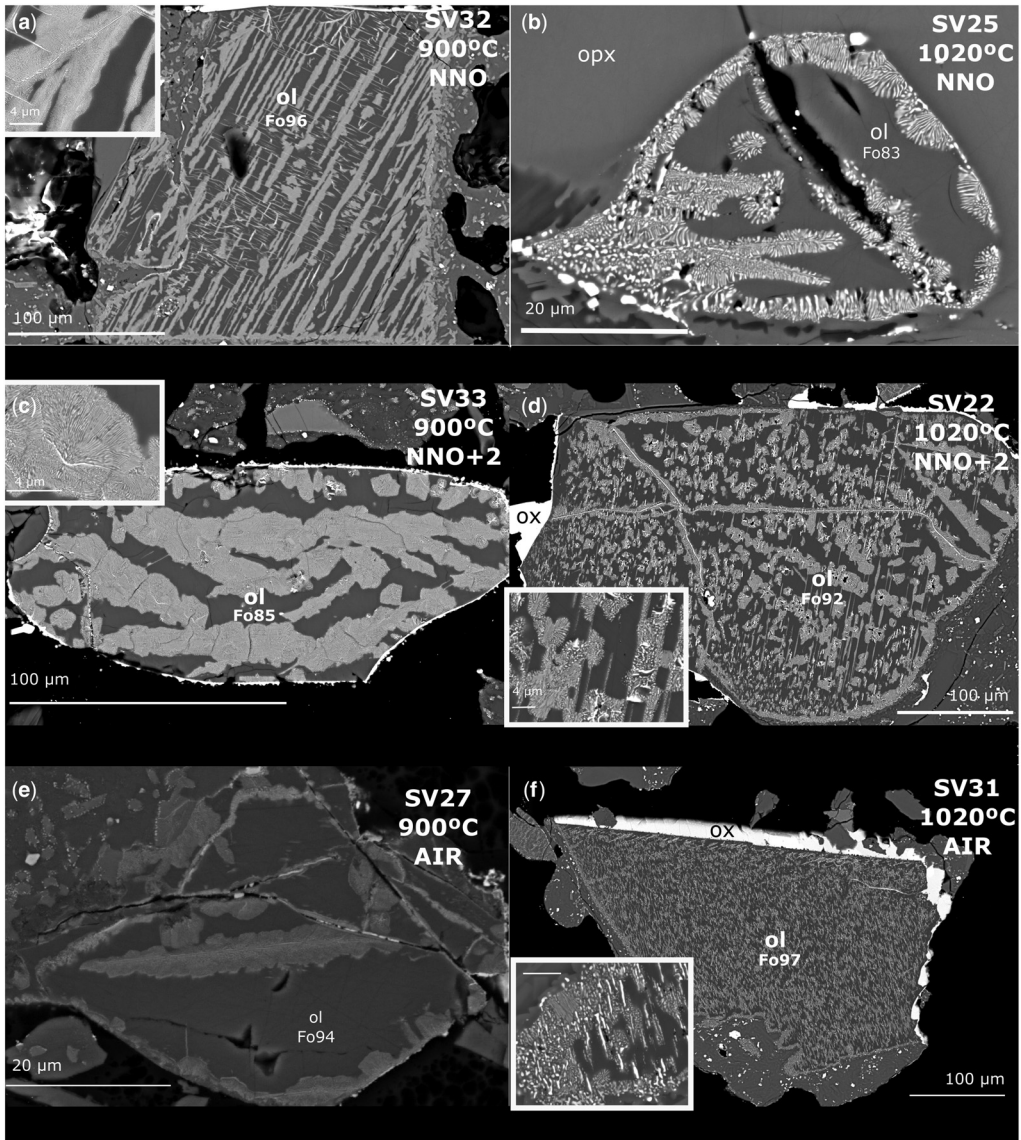


Fig. 6. BSE images of symplectite exsolution in olivine phenocrysts from experiments. (a) Linear bands of fine symplectite exsolution across the crystal interior. (b) Symplectite ‘blebs’ exsolving along the rim of an olivine intergrowth within an orthopyroxene grain. (c) Coarse symplectite exsolution bands, with Fe-oxides exsolving as well-developed fibrous budding lobes (see inset). (d) Clusters of symplectite exsolution, connected by thin rods of exsolved Fe-oxide. (e) Well-developed fibrous and budding symplectite lobes following the edge of the crystal and along a single band in the centre. (f) Ubiquitous symplectite exsolution, with clusters of symplectite ‘blebs’. Some olivine crystals also show an irregular oxide diffusion rim (white in BSE; high-Z) around the edge of the crystal. Forsterite of olivine host (Fo) calculated in moles as $\text{Mg} / (\text{Mg} + \text{Fe} + \text{Mn})$ crystal. Abbreviations as in Figure 1.

Iron–titanium oxide phenocrysts. Run product exsolved oxides contain variable amounts of Fe and Ti, and minor amounts of Mg, Al and Mn. In Figure 8 Fe–Ti oxides are plotted in terms of their quadrivalent, trivalent and divalent cations

$((\text{Ti}^{4+}) - (\text{Al}^{3+} + \text{Fe}^{3+}) - (\text{Mg}^{2+} + \text{Fe}^{2+} + \text{Mn}^{2+}))$ on a ternary diagram, along with oxides from the natural dome and scoria. Oxide formulae were recalculated as cations per 12 oxygens. All host oxides (solid symbols) form part of the titanomagnetite

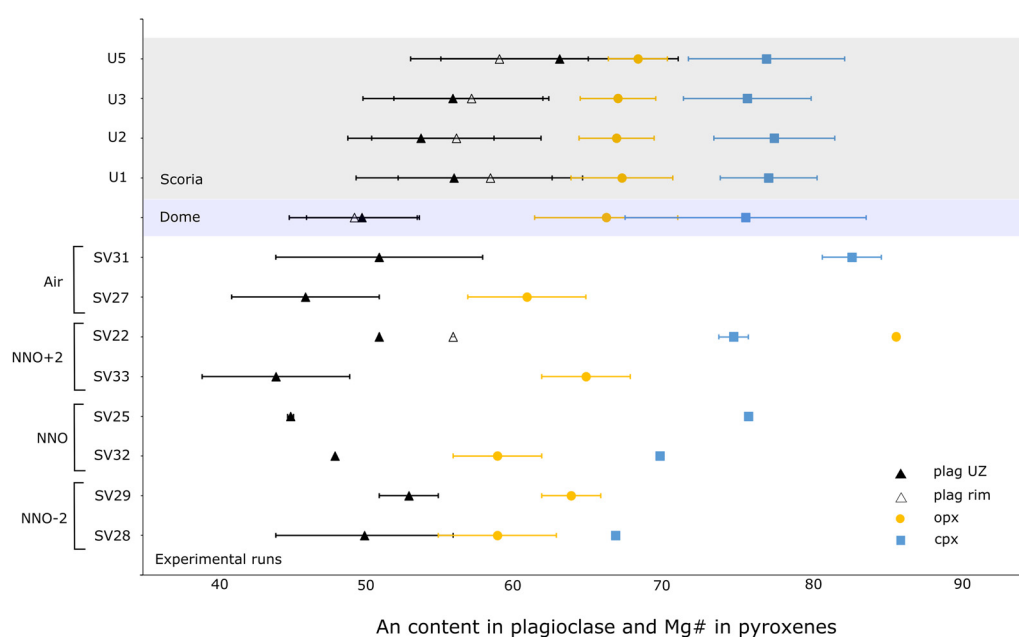


Fig. 7. Plagioclase and pyroxene microlite compositions in experimental run products, the natural dome, and scoria samples. Dome and scoria microlite data from Frey *et al.* (2023). Anorthite (An) content of unzoned plagioclase microlites plotted as solid black triangles, with new rim growth of zoned plagioclase microlites plotted as open black triangles. Mg# of orthopyroxene and clinopyroxene microlites plotted as yellow circles and blue squares, respectively. Error bars to one standard deviation. An content calculated as mol% Ca/(Ca + Na). Mg# calculated as cation fraction $\text{Mg}^{2+}/(\text{Mg}^{2+} + \text{Fe}^{2+})$.

spinel solid solution series, plotting along the ulvöspinel–magnetite join. Two main exsolution phases are identified: the first is a Ti-rich titanohematite rhombohedral oxide that plots along the ilmenite–hematite solid solution (open symbols); the second is a Ti-poor Mg–Fe–Al cubic spinel (pleonaste–magnesioferrite) that plots towards the base of the quadrilateral (open symbols). Exsolved titanohematites contain *c.* 33–43 wt% TiO_2 (Table 4) and exsolve as small granules or as vermicular exsolution lamellae in all experimental runs, except SV29 and SV25. The Mg–Fe–Al spinel phase is rich in Mg^{2+} (5–11 wt% MgO), Fe^{3+} (47–60 wt% Fe_2O_3 , calculated by stoichiometry) and Al^{3+} (6–15 wt% Al_2O_3), but is depleted in Ti^{4+} (< 3 wt% TiO_2), consistent with magnesioferrite–pleonaste stoichiometry (MgFe_2O_4 – $\text{Mg}_x\text{Fe}_{1-x}\text{Al}_2\text{O}_4$). The Mg–Fe–Al spinel exsolution phase, hereafter referred to as ‘magnesioferrite-rich spinel’, is found in both temperature series at NNO + 2, but only at 900°C in the presence of air. The lack of magnesioferrite-rich spinel in the most oxidizing experimental environment (in air at 1020°C) suggests a preference for titanohematite exsolution under these conditions. Experimental runs exsolving both titanohematite and magnesioferrite-rich spinel form assemblages where three compositionally distinct oxides co-exist,

shown as triangles in Figure 8. Host titanomagnetites are Al-poor (<6 wt% Al_2O_3), driving the exsolving magnesioferrite-rich spinel to incorporate a high proportion of Fe^{3+} .

Oxides in experimental runs at 900°C, at NNO + 2 and in air (SV22, SV27) are compositionally the most similar to the natural 2020–21 St Vincent dome rock regarding both host and exsolved magnesioferrite-rich spinel phases (Fig. 8). Exsolved titanohematite compositions in the experimental runs are more variable and depleted in Fe^{3+} compared to the dome (Fig. 8), likely due to the coeval exsolution of a magnesioferrite-rich spinel phase sequestering Fe^{3+} . Although the oxides analysed in the dome were not found to simultaneously exsolve titanohematite and magnesioferrite-rich spinel, all three of these oxide phases co-exist in the same rock sample (Fig. 1f). These three-oxide assemblages are represented by a dashed triangle in Figure 8. All experimentally-defined three-oxide assemblage triangles enclose one of the original scoria oxide compositions, supporting exsolution from an initially homogenous Fe–Ti oxide crystal, formed under conditions that were hotter and more reduced (blue shading; Fig. 2) than the experiments in which exsolution occurred. At one atmosphere pressure, the production and subsequent co-existence of three distinct

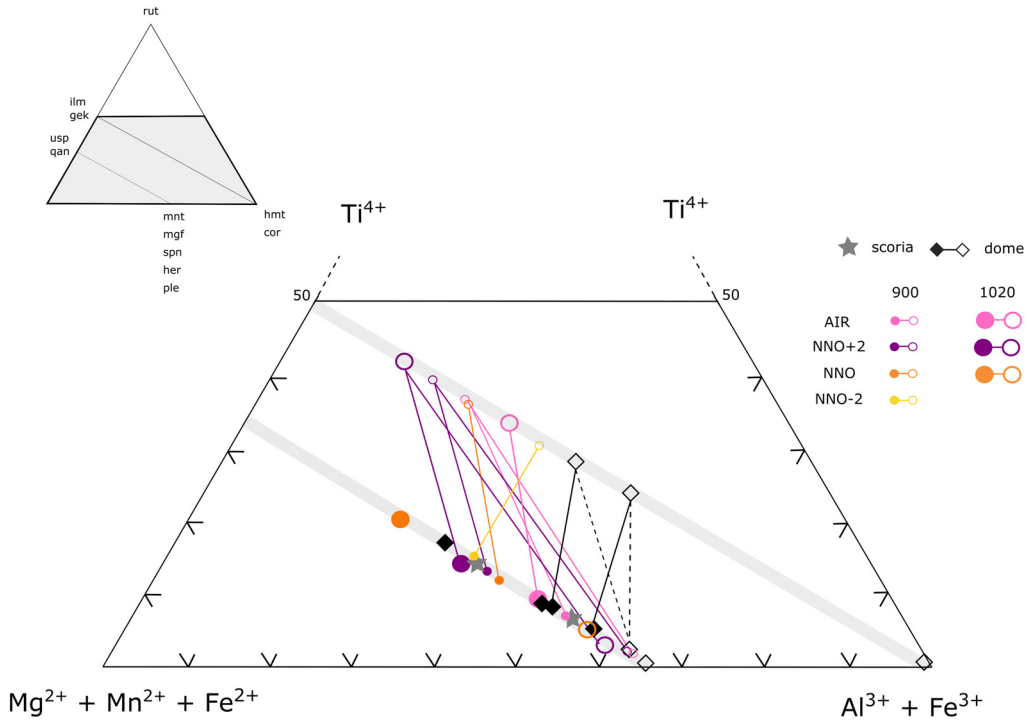


Fig. 8. Fe–Ti oxide compositions in experimental run products and natural dome and U3 scoria samples, plotted in ternary space depending on their number of quadri-, tri- and di- valent cations: $(\text{Ti}^{4+})-(\text{Al}^{3+} + \text{Fe}^{3+})-(\text{Mg}^{2+} + \text{Fe}^{2+} + \text{Mn}^{2+})$ per 12 oxygens normalized to a percentage. Host crystals are plotted as solid symbols and exsolved phases as open symbols. Low temperature experiments are shown as small circles, high temperature experiments as larger circles, with different colours for different oxygen fugacities; the natural dome rock shown as black diamonds and scoria as grey stars. Rhombohedral oxides (8 cations per 12 oxygens) plot along the ilmenite–hematite solid solution; cubic oxides (9 cations per 12 oxygens) plot along the ulvöspinel–magnetite solid solution. Host and exsolved oxides are connected by tie lines, with phases on the ulvöspinel–magnetite solid solution line assumed to be connected. Host oxides exsolving two different phases form three-oxide assemblage triangles, only present in the experiments at $\geq \text{NNO} + 2$ (pink and purple circles) and in the natural dome (black diamonds). Dashed lines connect oxides present in the same sample, but do not represent host and exsolved phases. Abbreviations as in Figure 2 as well as: gek, geikielite; qan, qandilite; cor, corundum; spn, spinel; her, hercynite; rut, rutile.

oxide phases is confined to temperatures below 1020°C and above NNO (Fig. 2). Only experiment SV27, at 900°C and in the presence of air, replicates both the textures and the compositions observed in the natural dome rock, forming well-developed trellis lamellae and recrystallization textures (Fig. 5). Thus, the T – $f\text{O}_2$ conditions of dome growth are inferred to lie close to those of experiment SV27 (pink shading; Fig. 2).

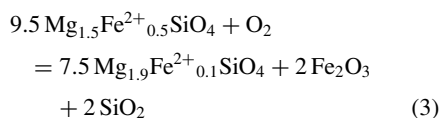
Olivine phenocrysts. Olivine crystals in experimental runs can be divided compositionally into two distinct groups, as seen in the natural starting material: the first with 0.6 wt% MnO and the second with 0.4 wt% MnO. All olivine crystals in experimental runs at and above the NNO buffer display symplectite exsolution and have high host crystal Fo

contents, ranging from Fo83–97 (Table 3). Host olivine crystals are enriched in Mg compared to the original composition of olivines in the scoria starting material (Fo65–75), due to the formation of Fe-oxide symplectites. The variation in Fo values in experiments reflects the degree of exsolution incurred and the proximity of analyses to the Fe-oxide symplectites within the crystal, indicative of a diffusive control on the reaction whereby temperature, $f\text{O}_2$ and time all play a role. Olivines subject to higher temperatures and $f\text{O}_2$ display more extensive symplectite exsolution, thus generating higher Fo contents in the host crystal (Fig. 6). Symplectitic olivines analysed in the dome have lower Fo contents than those in experimental runs (Fo74–82, Fig. 1h), suggesting more limited diffusion and exsolution, either over a shorter timescale or at lower

temperatures. The low Fo contents (Fo55) of the olivine microlite analysed in experiment SV29, at 1020°C and NNO – 2, is considerably Mg-poor compared to olivine microlites in the scoria (Fo71, Table 2; Frey *et al.* 2023), thus supporting new growth during experimental runs.

The compositions of the exsolving Fe-oxide symplectites could not be analysed directly due to their small grain size (<1 µm), but the co-existence of high-Fo olivine and absence of orthopyroxene implies the formation of hematite, as described earlier and reported in previous experimental studies (Haggerty and Baker 1967; Champness 1970; Gualtieri *et al.* 2003; Del Moro *et al.* 2013; Knafelc *et al.* 2019). Analysis of the oxide diffusion rims observed in SV33, SV22 and SV31 finds both magnesioferrite and hematite to be present, on the basis of stoichiometry. Well-developed diffusion rims effectively sequester Fe³⁺ and Mg, and suggest high degrees of oxidation, with their thickness and complexity reflecting the duration of oxidation (Haggerty and Baker 1967; Venezky and Rutherford 1999). Their absence in the St Vincent dome may reflect again different oxidation timescales between experimental runs and the natural dome.

Using the composition of the 0.4 wt% MnO unaltered olivine (Fo75) in the scoria as that of the original mineral prior to oxidation, equation (3) is a balanced reaction that describes the oxidation–exsolution reaction in experiment SV27, forming Fo94 olivine (with 0.4 wt% MnO), hematite and melt (SiO₂).



Discussion

Results presented in this study show that the alteration textures observed in the St Vincent 2020–21 lava dome are the products of high-temperature oxidation of basaltic andesite magma. As noted above, three main processes are capable of oxidizing a magma at or near the Earth's surface: deuteric oxidation, hydrothermal alteration or interaction with air.

Oxidation mechanism

Deuteric oxidation of magmas can result from degassing or crystallization. The magnitude of the $f\text{O}_2$ increase depends on the amount of H₂O exsolved and the amount of oxidizable Fe²⁺ in the magma. For the case of Fe-poor rhyolites (c. 1 wt% FeO^T) with 5.5 wt% H₂O, oxidation induced by degassing is of the order + 2 log $f\text{O}_2$ units (Burgisser and

Scaillet 2007) corresponding to conversion of c. 0.3 wt% FeO to Fe₂O₃. For Fe-rich basaltic andesite magmas (c. 8 wt% FeO^T; Table 1) with 4–6 wt% H₂O (Weber *et al.* 2023) the effect will be considerably less, on the order of + 0.3 log $f\text{O}_2$ units to oxidize the same amount of FeO. Sulfur degassing tends to counteract the effect of H₂O degassing depending on the initial redox state and sulfur content (Carmichael and Ghiorso 1986; Burgisser and Scaillet 2007). Sulfur contents of La Soufrière, St Vincent melt inclusions, from the 1979 eruption, are in the range 320–560 ppm (Devine and Sigurdsson 1983). Data for the 2021 scoria are even lower (40–270 ppm; Weber *et al.* 2023). Degassing this amount of sulfur would largely counterbalance any oxidative effect of H₂O degassing (Burgisser and Scaillet 2007). Thus, deuteric oxidation during dome magma degassing is not capable of delivering the high $f\text{O}_2$ required to generate the observed oxidation textures. We cannot rule out oxidation by streaming through the dome magma a much larger mass of SO₂-rich gas from deeper in the magmatic system, although low SO₂ degassing fluxes prior to and during dome extrusion (Joseph *et al.* 2022) and lack of abundant sulfides suggest this is unlikely.

Hydrothermal fluids can also oxidize a magma via the reduction of externally-derived H₂O. The composition of the fluid determines the extent of $f\text{O}_2$ change, as hydrothermal fluids may contain other redox species, such as sulfur (Binder and Keppler 2011; Ueda *et al.* 2021). Temperature estimates for hydrothermal alteration range from 50 to 500°C (Ball *et al.* 2013, 2015; Darmawan *et al.* 2022), requiring over 60 years for Fe–Ti oxides to fully re-equilibrate and achieve diffusion on length-scales of more than 20 µm (Venezky and Rutherford 1999). Prior to the 2020–21 eruption at La Soufrière, the last volcanic activity occurred in 1979, meaning any remnant magmas from this eruption have had only 40 years to re-equilibrate (Graham and Thirlwall 1981; Huppert *et al.* 1982). Hydrothermal alteration typically results in the precipitation of hydrous minerals such as chlorite and clay within three years, at shallow depths (Humphris 1976; Ball *et al.* 2013; Heap *et al.* 2019), as well as the breakdown of clinopyroxene, plagioclase and orthopyroxene (Austheim and Robins 1981; Boland and Otten 1985; Del Moro *et al.* 2013). The absence of such key features in the St Vincent dome samples suggests that hydrothermal fluids are unlikely to be responsible for generating the oxidation textures observed either in the conduit prior to eruption or on the crater floor.

Magmas oxidize readily at Earth's surface; however, the extent of oxidation and textures formed are temperature dependent (Buddington and Lindsley 1964; Haggerty and Baker 1967; Burkhard 2001; Del Moro *et al.* 2013; Gualtieri *et al.* 2003). For magmas to undergo extensive oxidation by air,

temperatures must remain high for reactions to be kinetically feasible ($>600^{\circ}\text{C}$, Burkhard 2001, 2005a; Del Moro *et al.* 2013; D'Oriano *et al.* 2013). The experimental results presented in this study illustrate that the dome-forming magma likely interacted with Earth's atmosphere at high temperatures to produce the well-developed trellis exsolution textures in Fe–Ti oxides that are seen in the dome (Figs 1f & 5e). Other alteration textures, including the development of olivine symplectites and rimming of pyroxene microlites and phenocrysts with oxides, occurring at and above NNO; with the exsolution of magnesioferrite-rich spinel from titanomagnetite requiring conditions $\geq \text{NNO} + 2$. The La Soufrière dome-forming magma therefore must have experienced oxidative conditions between $\text{NNO} + 2$ and air to form both the textures and compositions of co-existing oxidized mineral phases. Further evidence for interaction with air includes the formation of olivine symplectites along grain boundaries (Haggerty 1976a; Gualtieri *et al.* 2003; Del Moro *et al.* 2013; Knafelc *et al.* 2019) and the nucleation of oxide nanolites on the rims of pyroxene crystals (D'Oriano *et al.* 2013, 2014; Matsumoto and Geshi 2021). Studies exploring the porosity and permeability of lava domes corroborate the possibility of heterogeneous airflow to dome interiors via pore spaces or microfractures (Colombier *et al.* 2017; Darmawan *et al.* 2022). The difficulty of sampling the dome in 2021 makes it hard to assess the original location of the sample studied, with respect to the original dome surface or internal cracks.

Temperature

The temperature range explored in this study ($900\text{--}1020^{\circ}\text{C}$) reflects magmatic temperature estimates from two-pyroxene thermometry for La Soufrière (Weber *et al.* 2023). The temperature of the dome exterior at the time of extrusion was measured at $590 \pm 12^{\circ}\text{C}$ from thermal imaging (Stinton 2023), providing a minimum temperature constraint for alteration at the Earth's surface. Reheating experiments in air illustrate the need for elevated temperatures to facilitate subsolidus oxidation, which would otherwise be kinetically inhibited (Venezky and Rutherford 1999; Blondes *et al.* 2012; D'Oriano *et al.* 2013, 2014). In past experiments oxide nanolites are initially formed at temperatures of 750°C , but only become predominant in the groundmass and rim pyroxene and plagioclase microlites, as we see in the St Vincent dome, at temperatures nearer 1000°C (D'Oriano *et al.* 2013).

Experimental runs at 900°C most closely replicate the symplectitic olivine textures in the natural dome, with exsolution restricted to grain boundaries and well-defined bands traversing the crystal. Experiments at 1020°C instead display extensive

exsolution throughout the crystal, illustrating the role of temperature in controlling the type and extent of symplectite exsolution produced. Olivine symplectites generally develop during sub-solidus oxidation ($<980\text{--}1060^{\circ}\text{C}$; Barton *et al.* 1991). At lower temperatures ($600\text{--}700^{\circ}\text{C}$), the intermediate phase laihunite ($\text{Fe}^{2+}\text{Fe}_2^{3+}(\text{SiO}_4)_2$) forms during oxidation (Khisina *et al.* 1995, 1998), whereas at higher temperatures Fe-rich olivine initially breaks down to form orthopyroxene and magnesioferrite as metastable phases. With continued heating ($>820^{\circ}\text{C}$), high-Fo olivine and hematite are produced (Haggerty and Baker 1967). The lack of laihunite and orthopyroxene in the St Vincent dome, suggests temperatures were above 820°C .

Fe–Ti oxides form a variety of solid solutions, each unmixing to form two (or rarely more) separate oxide phases during sub-solidus exsolution at a unique consolute temperature (Haggerty 1976a). Previous experimental studies identify the magnetite–hematite consolute temperature to be between 527 and 600°C (Kawai *et al.* 1954; Vincent *et al.* 1957; Lilova *et al.* 2012); the magnetite–hercynite and magnetite–pleonaste consolute temperatures to be *c.* 860°C and *c.* 900°C , respectively (Turnock and Eugster 1962; Tan *et al.* 2016), and the ulvöspinel–hercynite and qandilite–spinel consolute temperatures to be *c.* 1300°C and *c.* 1370°C , respectively (Muan *et al.* 1972; Ghiorso and Sack 1991; Lindsley 1991). The temperatures at which magnesioferrite-rich spinel and titanohematite exsolve from titanomagnetite, as seen in this study, have not previously been established. Our results experimentally constrain the exsolution of such phases to temperatures above 900°C in the presence of air and above 1020°C at $\text{NNO} + 2$ (Fig. 2). The exsolved phases are rich in Fe^{3+} , indicative of significant oxidation (Haggerty 1976a). Sub-solvus exsolution often occurs during slow cooling when Fe–Ti oxides re-equilibrate (Hammond and Taylor 1982); however, super-solvus oxidation–exsolution is possible in extremely oxidizing conditions whereby newly-formed (more oxidized) components are excluded from the original host crystal lattice (Von Gruenewaldt *et al.* 1985; Arguin *et al.* 2018). Collectively the oxidation textures observed in the St Vincent dome define the minimum temperature of oxidation to be between 750 and 820°C , from the abundance of oxide-rimmed microlites in the groundmass and exsolution of hematite symplectites from olivine. The breakdown of orthopyroxene at 1020°C , at and above NNO, identified in this study, provides an upper temperature limit of *c.* 900°C .

Timescale

The experiments presented in this study suggest that the oxidation textures observed in the St Vincent

dome most likely formed within a week at temperatures $\leq 900^{\circ}\text{C}$, at the Earth's surface. Fe–Ti oxides re-equilibrate very quickly with re-equilibration timescales dependent on the temperature, ranging from 50 hours at 1000°C to 60 years at 600°C (Hammond and Taylor 1982; Gardner *et al.* 1995; Venetzky and Rutherford 1999; Hou *et al.* 2021). Previous experimental studies using more fayalite-rich olivine also found that rapid heating in air between 820 and 1000°C results in the continuous breakdown of the original olivine to hematite and high-Fo olivine, whereas slower heating forms orthopyroxene and magnesioferrite (Champness 1970). This observation supports rapid high-temperature oxidation of the St Vincent dome. The lack of oxide diffusion rims around symplectitic olivines, formed during prolonged oxidation periods, further suggests that oxidation at La Soufrière could have occurred on timescales of less than a week, the duration of experimental runs (Haggerty and Baker 1967). However, we cannot rule out longer oxidation timescales at slightly lower temperatures (750 – 820°C , as suggested above), but these are unlikely to have exceeded the twenty days between extrusion and sampling.

Conclusions

Petrological monitoring of the La Soufrière 2020–21 lava dome, combined with the results from heating and oxidation experiments presented in this study, show that the textures of the dome rock are best explained by oxidation in the presence of air at temperatures $\leq 900^{\circ}\text{C}$ on timescales of weeks. Oxide nanolites are found to nucleate on the rims of pyroxene microlites and orthopyroxene phenocrysts in all experiments $\geq \text{NNO}$. Orthopyroxene phenocrysts become unstable at 1020°C and one atmosphere $\geq \text{NNO}$. The composition of exsolved Fe–Ti oxides and olivines in the natural dome rock match those in experimental runs at 900°C at $\text{NNO} + 2$ and in air, suggesting an intermediate or fluctuating oxidation state. However, certain exsolution textures, such as Fe–Ti oxide trellis lamellae and recrystallization, are only replicated experimentally in the presence of air at 900°C (Fig. 5e). In higher temperature runs (1020°C), Fe–Ti oxides and olivines are considerably more altered than those observed in the dome, implying an upper temperature limit of dome oxidation at 900°C (Fig. 2).

The experiments presented in this study demonstrate that oxidation–exsolution reactions can occur relatively quickly (< 168 h), particularly in the presence of air and at sustained high temperatures. The textures observed in the La Soufrière 2020–21 lava dome are therefore inferred to have developed at the surface during dome emplacement, rather than during long-term magma sub-surface storage prior

to eruption. Use of the U3 scoria as starting material and its ability to reproduce dome phenocryst textures experimentally suggests that, plausibly, both dome and scoria could be sourced from the same basaltic andesite magma batch. This possibility is supported by near-identical bulk rock and phenocryst assemblages, but with distinct post-eruptive cooling histories. On the basis of the experimental results, the characteristic alteration textures of the 2020–21 La Soufrière dome are considered to be post- or syn-emplacement oxidation features; however, the limited number of samples from the active dome preclude any assessment of whether the observed textures are ubiquitous or confined to the surface of the dome at the sampling site.

Acknowledgements We thank Gregor Weber, Holli Frey and Matthew Manon for sharing their data, as well as Jenni Barclay, Steve Sparks and Kathy Cashman for useful discussions. Thank you to Michal Camejo-Harry for providing feedback on the initial manuscript. We thank our reviewers Martin Mangler and Holli Frey for their helpful and constructive comments. We are also grateful to Andrew Matzen for help with EPMA. The authors acknowledge use of characterization facilities within the David Cockayne Centre for Electron Microscopy, Department of Materials, University of Oxford. We also thank Julien Boulliung and Bernie Wood for valuable input in the experimental laboratory.

Competing interests The authors declare that they have no known competing financial interests or personal relationships that could have appeared to influence the work reported in this paper.

Author contributions BME: conceptualization (supporting), formal analysis (lead), investigation (lead), methodology (lead), writing – original draft (lead), writing – review & editing (equal); EM: conceptualization (supporting), formal analysis (supporting), investigation (supporting), supervision (equal), writing – review & editing (equal); JB: conceptualization (lead), investigation (supporting), supervision (equal), writing – review & editing (equal).

Funding BM-E acknowledges a PhD studentship supported by the Royal Society Research Professorship awarded to JB (grant ref RP/R1\201048) and by University College, Oxford. The authors acknowledge financial support provided by the Henry Royce Institute (grant ref EP/R010145/1).

Data availability All data generated and analysed in this study are provided in the results section of this paper. Additional data supporting this study are available in Weber *et al.* (2023) and Frey *et al.* (2023).

References

- Anderson, A. and Wright, T. 1972. Phenocrysts and glass inclusions and their bearing on oxidation and mixing of basaltic magmas, Kilauea volcano, Hawaii. *American Mineralogist: Journal of Earth and Planetary Materials*, **57**, 188–216.
- Arguin, J.-P., Pagé, P., Barnes, S.-J., Girard, R. and Duran, C. 2018. An integrated model for ilmenite, Al-spinel, and corundum exsolutions in titanomagnetite from oxide-rich layers of the Lac Doré Complex (Québec, Canada). *Minerals*, **8**, 476, <https://doi.org/10.3390/min8110476>
- Austrheim, H. and Robins, B. 1981. Reactions involving hydration of orthopyroxene in anorthosite-gabbro. *Lithos*, **14**, 275–281, [https://doi.org/10.1016/0024-4937\(81\)90055-4](https://doi.org/10.1016/0024-4937(81)90055-4)
- Bain, A.A., Kendrick, J.E. *et al.* 2021. Micro-textural controls on magma rheology and vulcanian explosion cyclicity. *Frontiers in Earth Science*, **8**, 611320, <https://doi.org/10.3389/feart.2020.611320>
- Ball, J.L., Calder, E.S., Hubbard, B.E. and Bernstein, M.L. 2013. An assessment of hydrothermal alteration in the Santiaguito lava dome complex, Guatemala: implications for dome collapse hazards. *Bulletin of Volcanology*, **75**, 676, <https://doi.org/10.1007/s00445-012-0676-z>
- Ball, J.L., Stauffer, P.H., Calder, E.S. and Valentine, G.A. 2015. The hydrothermal alteration of cooling lava domes. *Bulletin of Volcanology*, **77**, 102, <https://doi.org/10.1007/s00445-015-0986-z>
- Barnes, S.J. and Roeder, P.L. 2001. The range of spinel compositions in terrestrial mafic and ultramafic rocks. *Journal of Petrology*, **42**, 2279–2302, <https://doi.org/10.1093/petrology/42.12.2279>
- Barton, M. and Van Gaans, C. 1988. Formation of orthopyroxene-Fe-Ti oxide symplectites in Precambrian intrusives, Rogaland, southwestern Norway. *American Mineralogist*, **73**, 1046–1059.
- Barton, M., Sheets, J.M., Lee, W.E. and van Gaans, C. 1991. Occurrence of low-Ca clinopyroxene and the role of deformation in the formation of pyroxene-Fe-Ti oxide symplectites. *Contributions to Mineralogy and Petrology*, **108**, 181–195, <https://doi.org/10.1007/BF00307337>
- Bell, P.M., Mao, H.K., Roedder, E. and Weiblen, P.W. 1975. The problem of the origin of symplectites in olivine-bearing lunar rocks. *Lunar and Planetary Science Conference Proceedings*, **1**, 231–248.
- Binder, B. and Keppler, H. 2011. The oxidation state of sulfur in magmatic fluids. *Earth and Planetary Science Letters*, **301**, 190–198, <https://doi.org/10.1016/j.epsl.2010.10.042>
- Blondes, M.S., Brandon, M.T., Reiners, P.W., Page, F.Z. and Kita, N.T. 2012. Generation of forsteritic olivine (Fo99.8) by subsolidus oxidation in basaltic flows. *Journal of Petrology*, **53**, 971–984, <https://doi.org/10.1093/petrology/egs006>
- Blundy, J., Melekhova, E. *et al.* 2020. Effect of redox on Fe-Mg-Mn exchange between olivine and melt and an oxybarometer for basalts. *Contributions to Mineralogy and Petrology*, **175**, 103, <https://doi.org/10.1007/s00410-020-01736-7>
- Boland, J.N. and Otten, M.T. 1985. Symplectitic augite: evidence for discontinuous precipitation as an exsolution mechanism in Ca-rich clinopyroxene. *Journal of Metamorphic Geology*, **3**, 13–20, <https://doi.org/10.1111/j.1525-1314.1985.tb00302.x>
- Boulliung, J., Füre, E., Dalou, C., Tissandier, L., Zimmermann, L. and Marrocchi, Y. 2020. Oxygen fugacity and melt composition controls on nitrogen solubility in silicate melts. *Geochimica et Cosmochimica Acta*, **284**, 120–133, <https://doi.org/10.1016/j.gca.2020.06.020>
- Brown, G.M., Holland, J.G., Sigurdsson, H., Tomblin, J.F. and Arculus, R.J. 1977. Geochemistry of the Lesser Antilles volcanic island arc. *Geochimica et Cosmochimica Acta*, **41**, 785–801, [https://doi.org/10.1016/0016-7037\(77\)90049-7](https://doi.org/10.1016/0016-7037(77)90049-7)
- Buddington, A.F. and Lindsley, D.H. 1964. Iron-titanium oxide minerals and synthetic equivalents. *Journal of Petrology*, **5**, 310–357, <https://doi.org/10.1093/petrology/5.2.310>
- Burgisser, A. and Scaillet, B. 2007. Redox evolution of a degassing magma rising to the surface. *Nature*, **445**, 194–197, <https://doi.org/10.1038/nature05509>
- Burkhard, D.J.M. 2001. Crystallization and oxidation of Kilauea basalt glass: processes during reheating experiments. *Journal of Petrology*, **42**, 507–527, <https://doi.org/10.1093/petrology/42.3.507>
- Burkhard, D.J.M. 2005a. Crystallization and oxidation during emplacement of lava lobes. *Geological Society of America Special Papers*, **396**, <https://doi.org/10.1130/0-8137-2396-5.67>
- Burkhard, D.J.M. 2005b. Nucleation and growth rates of pyroxene, plagioclase, and Fe-Ti oxides in basalt under atmospheric conditions. *European Journal of Mineralogy*, **17**, 675–686, <https://doi.org/10.1127/0935-1221/2005/0017-0675>
- Calder, E.S., Lavallée, Y., Kendrick, J.E. and Bernstein, M. 2015. Lava dome eruptions. In: *The Encyclopedia of Volcanoes*. Academic Press, 343–362, <https://doi.org/10.1016/B978-0-12-385938-9.00018-3>
- Canil, D. 1994. Stability of clinopyroxene at pressure-temperature conditions of the transition region. *Physics of the Earth and Planetary Interiors*, **86**, 25–34, [https://doi.org/10.1016/0031-9201\(94\)05059-7](https://doi.org/10.1016/0031-9201(94)05059-7)
- Carmichael, I.S.E. 1991. The redox states of basic and silicic magmas: a reflection of their source regions? *Contributions to Mineralogy and Petrology*, **106**, 129–141, <https://doi.org/10.1007/BF00306429>
- Carmichael, I.S.E. and Ghiorso, M.S. 1986. Oxidation-reduction relations in basic magma: a case for homogeneous equilibria. *Earth and Planetary Science Letters*, **78**, 200–210, [https://doi.org/10.1016/0012-821X\(86\)90061-0](https://doi.org/10.1016/0012-821X(86)90061-0)
- Carr, B. 2016. *Transitions in Eruption Style at Silicic Volcanoes: From Stable Domes to Pyroclastic Flows and Explosive Plumes*. Arizona State University.
- Cashman, K.V. 1992. Groundmass crystallization of Mount St. Helens dacite, 1980–1986: a tool for interpreting shallow magmatic processes. *Contributions to Mineralogy and Petrology*, **109**, 431–449, <https://doi.org/10.1007/BF00306547>
- Cashman, K. and Blundy, J. 2000. Degassing and crystallization of ascending andesite and dacite. *Philosophical Transactions of the Royal Society of London. Series A: Mathematical, Physical and Engineering Sciences*, **358**, 1487–1513, <https://doi.org/10.1098/rsta.2000.0600>

- Cassidy, M., Trofimovs, J. *et al.* 2014. Chapter 20 Multi-stage collapse events in the South Soufrière Hills, Montserrat as recorded in marine sediment cores. *Geological Society, London, Memoirs*, **39**, 383–397, <https://doi.org/10.1144/M39.20>
- Cassidy, M., Ebmeier, S.K. *et al.* 2019. Explosive eruptions with little warning: experimental petrology and volcano monitoring observations from the 2014 eruption of Kelud, Indonesia. *Geochemistry, Geophysics, Geosystems*, **20**, 4218–4247, <https://doi.org/10.1029/2018GC008161>
- Champness, P.E. 1970. Nucleation and growth of iron oxides in olivines, (Mg,Fe)₂SiO₄. *Mineralogical Magazine*, **37**, 790–800, <https://doi.org/10.1180/minmag.1970.037.291.05>
- Cole, P.D., Robertson, R.E.A., Fedele, L. and Scarpato, C. 2019. Explosive activity of the last 1000 years at La Soufrière, St Vincent, Lesser Antilles. *Journal of Volcanology and Geothermal Research*, **371**, 86–100, <https://doi.org/10.1016/j.jvolgeores.2019.01.002>
- Cole, P.D., Barclay, J. *et al.* 2023. Explosive sequence of La Soufrière, St Vincent, April 2021: insights into drivers and consequences via eruptive products. *Geological Society, London, Special Publications*, **539**, <https://doi.org/10.1144/SP539-2022-292>
- Colombier, M., Wadsworth, F.B., Gurioli, L., Scheu, B., Kueppers, U., Di Muro, A. and Dingwell, D.B. 2017. The evolution of pore connectivity in volcanic rocks. *Earth and Planetary Science Letters*, **462**, 99–109, <https://doi.org/10.1016/j.epsl.2017.01.011>
- Costa, F., Andreastuti, S., Bouvet de Maisonneuve, C. and Pallister, J.S. 2013. Petrological insights into the storage conditions, and magmatic processes that yielded the centennial 2010 Merapi explosive eruption. *Journal of Volcanology and Geothermal Research*, **261**, 209–235, <https://doi.org/10.1016/j.jvolgeores.2012.12.025>
- Cottrell, E., Gardner, J.E. and Rutherford, M.J. 1999. Petrologic and experimental evidence for the movement and heating of the pre-eruptive Minoan rhyodacite (Santorini, Greece). *Contributions to Mineralogy and Petrology*, **135**, 315–331, <https://doi.org/10.1007/s004100050514>
- Creer, K.M., Ibbetson, J. and Drew, W. 1970. Activation energy of cation migration in titanomagnetites. *Geophysical Journal International*, **19**, 93–101, <https://doi.org/10.1111/j.1365-246X.1970.tb06740.x>
- Darmawan, H., Troll, V.R. *et al.* 2022. Hidden mechanical weaknesses within lava domes provided by buried high-porosity hydrothermal alteration zones. *Scientific Reports*, **12**, 3202, <https://doi.org/10.1038/s41598-022-06765-9>
- Deardorff, N. and Cashman, K. 2017. Rapid crystallization during recycling of basaltic andesite tephra: timescales determined by reheating experiments. *Scientific Reports*, **7**, 46364, <https://doi.org/10.1038/srep46364>
- Deines, P., Nafziger, R.H., Ulmer, G.C. and Woermann, E. 1976. Temperature–oxygen fugacity tables for selected gas mixtures in the system C–H–O at one atmosphere total pressure. *Metallurgical and Materials Transactions B*, **7**, 143–143, <https://doi.org/10.1007/BF02652831>
- Del Moro, S., Renzulli, A., Landi, P., La Felice, S. and Rosi, M. 2013. Unusual lapilli tuff ejecta erupted at Stromboli during the 15 March 2007 explosion shed light on the nature and thermal state of rocks forming the crater system of the volcano. *Journal of Volcanology and Geothermal Research*, **254**, 37–52, <https://doi.org/10.1016/j.jvolgeores.2012.12.017>
- Devine, J.D. and Sigurdsson, H. 1983. The liquid composition and crystallization history of the 1979 Soufrière magma, St. Vincent, W.I. *Journal of Volcanology and Geothermal Research*, **16**, 1–31, [https://doi.org/10.1016/0377-0273\(83\)90082-3](https://doi.org/10.1016/0377-0273(83)90082-3)
- Dirksen, O., Humphreys, M.C.S., Pletchov, P., Melnik, O., Demyanchuk, Y., Sparks, R.S.J. and Mahony, S. 2006. The 2001–2004 dome-forming eruption of Shiveluch volcano, Kamchatka: Observation, petrological investigation and numerical modelling. *Journal of Volcanology and Geothermal Research*, **155**, 201–226, <https://doi.org/10.1016/j.jvolgeores.2006.03.029>
- D’Oriano, C., Pompilio, M., Bertagnini, A., Cioni, R. and Pichavant, M. 2013. Effects of experimental reheating of natural basaltic ash at different temperatures and redox conditions. *Contributions to Mineralogy and Petrology*, **165**, 863–883, <https://doi.org/10.1007/s00410-012-0839-0>
- D’Oriano, C., Bertagnini, A., Cioni, R. and Pompilio, M. 2014. Identifying recycled ash in basaltic eruptions. *Scientific Reports*, **4**, 5851, <https://doi.org/10.1038/srep05851>
- Duchesne, J.-C. 1972. Iron–Titanium oxide minerals in the Bjerkrem-Sogndal Massif, south-western Norway. *Journal of Petrology*, **13**, 57–81, <https://doi.org/10.1093/petrology/13.1.57>
- Edmonds, M. and Herd, R.A. 2007. A volcanic degassing event at the explosive–effusive transition. *Geophysical Research Letters*, **34**, L21310, <https://doi.org/10.1029/2007GL031379>
- Ejima, T., Akasaka, M., Nagao, T. and Ohfuji, H. 2013. Oxidation states of Fe and precipitates within olivine from orthopyroxene–olivine–clinopyroxene andesite lava from Kasayama volcano, Hagi, Yamaguchi, Japan. *Journal of Mineralogical and Petrological Sciences*, **108**, 25–36, <https://doi.org/10.2465/jmps.120621a>
- Ejima, T., Yoneda, M., Akasaka, M., Ohfuji, H., Kon, Y., Nagashima, M. and Nakamuta, Y. 2017. Precipitates within olivine phenocrysts in oxidized andesitic scoria from Kasayama volcano, Hagi, Japan. *Journal of Mineralogical and Petrological Sciences*, **112**, 116–126, <https://doi.org/10.2465/jmps.161219>
- Evans, B.W., Scaillet, B. and Kuehner, S.M. 2006. Experimental determination of coexisting iron–titanium oxides in the systems FeTiAlO, FeTiAlMgO, FeTiAlMnO, and FeTiAlMgMnO at 800 and 900°C, 1–4 kbar, and relatively high oxygen fugacity. *Contributions to Mineralogy and Petrology*, **152**, 149–167, <https://doi.org/10.1007/s00410-006-0098-z>
- Fedele, L., Cole, P.D., Scarpato, C. and Robertson, R.E.A. 2021. Petrological insights on the last 1000 years of explosive activity at La Soufrière volcano, St. Vincent (Lesser Antilles). *Lithos*, **392**, 106150, <https://doi.org/10.1016/j.lithos.2021.106150>
- Fink, J.H. and Griffiths, R.W. 1998. Morphology, eruption rates, and rheology of lava domes: Insights from laboratory models. *Journal of Geophysical Research: Solid*

- Earth*, **103**, 527–545, <https://doi.org/10.1029/97JB02838>
- Fink, J.H., Malin, M.C. and Anderson, S.W. 1990. Intrusive and extrusive growth of the Mount St Helens lava dome. *Nature*, **348**, 435–437, <https://doi.org/10.1038/348435a0>
- Freer, R. and Hauptman, Z. 1978. An experimental study of magnetite–titanomagnetite interdiffusion. *Physics of the Earth and Planetary Interiors*, **16**, 223–231, [https://doi.org/10.1016/0031-9201\(78\)90015-8](https://doi.org/10.1016/0031-9201(78)90015-8)
- Freer, W. and O'Reilly, R. 1980. The diffusion of Fe²⁺ ions in spinels with relevance to the process of magnetization. *Mineralogical Magazine*, **43**, 889–899, <https://doi.org/10.1180/minmag.1980.043.331.12>
- Frey, H.M., Manon, M.R. et al. 2023. Petrology of the explosive deposits from the April 2021 eruption of La Soufrière volcano, St Vincent: a time-series analysis of microlites. *Geological Society, London, Special Publications*, **539**, <https://doi.org/10.1144/SP539-2022-291>
- Frost, B.R. 1991. Magnetic petrology; factors that control the occurrence of magnetite in crustal rocks. *Reviews in Mineralogy and Geochemistry*, **25**, 489–509.
- Frost, B.R. and Lindsley, D.H. 1991. Occurrence of iron–titanium oxides in igneous rocks. In: Lindsley, D.H. (ed.) *Oxide Minerals*. De Gruyter, 433–468, <https://doi.org/10.1515/9781501508684-015>
- Gaetani, G., Grove, T. et al. 1994. 32. Experimental phase relations of basaltic andesite from Hole 839B under hydrous and anhydrous conditions. *Proceedings of the Ocean Drilling Program, Scientific Results*, **135**, <https://doi.org/10.2973/odp.proc.sr.135.1994>
- Gardner, J.E., Carey, S., Rutherford, M.J. and Sigurdsson, H. 1995. Petrologic diversity in Mount St. Helens dacites during the last 4,000 years: implications for magma mixing. *Contributions to Mineralogy and Petrology*, **119**, 224–238, <https://doi.org/10.1007/BF00307283>
- Genareau, K. and Clarke, A.B. 2010. Heterogeneous clasts as windows into magma mingling at Soufrière Hills volcano: Small-scale magma mingling processes. *Geophysical Research Letters*, **37**, <https://doi.org/10.1029/2009GL041968>
- Ghiorso, M.S. and Sack, O. 1991. Fe–Ti oxide geothermometry: thermodynamic formulation and the estimation of intensive variables in silicic magmas. *Contributions to Mineralogy and Petrology*, **108**, 485–510, <https://doi.org/10.1007/BF00303452>
- Goode, A.D.T. 1974. Oxidation of natural olivines. *Nature*, **248**, 500–501, <https://doi.org/10.1038/248500a0>
- Gorbach, N., Filosofova, T. and Portnyagin, M. 2020. Amphibole record of the 1964 plinian and following dome-forming eruptions of Shiveluch volcano, Kamchatka. *Journal of Volcanology and Geothermal Research*, **407**, 107108, <https://doi.org/10.1016/j.jvolgeores.2020.107108>
- Graham, A.M. and Thirlwall, M.F. 1981. Petrology of the 1979 eruption of Soufrière volcano, St. Vincent, Lesser Antilles. *Contributions to Mineralogy and Petrology*, **76**, 336–342, <https://doi.org/10.1007/BF00375460>
- Grocke, S.B., Cottrell, E., de Silva, S. and Kelley, K.A. 2016. The role of crustal and eruptive processes v. source variations in controlling the oxidation state of iron in Central Andean magmas. *Earth and Planetary Science Letters*, **440**, 92–104, <https://doi.org/10.1016/j.epsl.2016.01.026>
- Grove, T.L. and Juster, T.C. 1989. Experimental investigations of low-Ca pyroxene stability and olivine–pyroxene–liquid equilibria at 1-atm in natural basaltic and andesitic liquids. *Contributions to Mineralogy and Petrology*, **103**, 287–305, <https://doi.org/10.1007/BF00402916>
- Gualtieri, A.F., Gemmi, M. and Dapiaggi, M. 2003. Phase transformations and reaction kinetics during the temperature-induced oxidation of natural olivine. *American Mineralogist*, **88**, 1560–1574, <https://doi.org/10.2138/am-2003-1019>
- Haggerty, S.E. 1976a. Oxidation of opaque mineral oxides in basalts. In: Rumble, D. (ed.) *Oxide Minerals*. De Gruyter, 113–212, <https://doi.org/10.1515/9781501508561-009>
- Haggerty, S.E. 1976b. Opaque mineral oxides in terrestrial igneous rocks. In: Rumble, D. (ed.) *Oxide Minerals*. De Gruyter, 303–502, <https://doi.org/10.1515/9781501508561-013>
- Haggerty, S.E. 1991. Oxide Textures – A Mini-Atlas. In: Lindsley, D.H. (ed.) *Oxide Minerals*. De Gruyter, 129–220, <https://doi.org/10.1515/9781501508684-008>
- Haggerty, S.E. and Baker, I. 1967. The alteration of olivine in basaltic and associated lavas: Part I: High temperature alteration. *Contributions to Mineralogy and Petrology*, **16**, 233–257, <https://doi.org/10.1007/BF00371094>
- Hammer, J.E., Cashman, K.V., Hoblitt, R.P. and Newman, S. 1999. Degassing and microlite crystallization during pre-climatic events of the 1991 eruption of Mt. Pinatubo, Philippines. *Bulletin of Volcanology*, **60**, 355–380, <https://doi.org/10.1007/s004450050238>
- Hammond, P.A. and Taylor, L.A. 1982. The ilmenite/titano-magnetite assemblage: kinetics of re-equilibration. *Earth and Planetary Science Letters*, **61**, 143–150, [https://doi.org/10.1016/0012-821X\(82\)90047-4](https://doi.org/10.1016/0012-821X(82)90047-4)
- Harford, C.L., Pringle, M.S., Sparks, R.S.J. and Young, S.R. 2002. The volcanic evolution of Montserrat using ⁴⁰Ar/³⁹Ar geochronology. *Geological Society, London, Memoirs*, **21**, 93–113, <https://doi.org/10.1144/GSL.MEM.2002.021.01.05>
- Harrison, R.J. and Putnis, A. 1998. The magnetic properties and crystal chemistry of oxide spinel solid solutions. *Surveys in Geophysics*, **19**, 461–520, <https://doi.org/10.1023/A:1006535023784>
- Heap, M.J., Troll, V.R. et al. 2019. Hydrothermal alteration of andesitic lava domes can lead to explosive volcanic behaviour. *Nature Communications*, **10**, 5063, <https://doi.org/10.1038/s41467-019-13102-8>
- Heath, E., Macdonald, R., Belkin, H., Hawkesworth, C. and Sigurdsson, H. 1998. Magmagenesis at Soufrière Volcano, St Vincent, Lesser Antilles Arc. *Journal of Petrology*, **39**, 1721–1764, <https://doi.org/10.1093/ptro/39.10.1721>
- Hekinian, R. 1982. Deuteric alteration. *Elsevier Oceanography Series*, **33**, 329–331, [https://doi.org/10.1016/S0422-9894\(08\)70953-X](https://doi.org/10.1016/S0422-9894(08)70953-X)
- Holloway, J.R. 2004. Redox reactions in seafloor basalts: possible insights into silicic hydrothermal systems. *Chemical Geology*, **210**, 225–230, <https://doi.org/10.1016/j.chemgeo.2004.06.009>

- Hou, T., Botcharnikov, R. *et al.* 2021. Kinetics of Fe–Ti oxide re-equilibration in magmatic systems: implications for thermo-oxybarometry. *Journal of Petrology*, **61**, egaal16, <https://doi.org/10.1093/petrology/egaal16>
- Humphris, S.E. 1976. *The Hydrothermal Alteration of Oceanic Basalts by Seawater*. Thesis, Woods Hole Oceanographic Institution, <https://doi.org/10.1575/1912/1351>
- Huppert, H.E., Shepherd, J.B., Haraldur Sigurdsson, R. and Sparks, S.J. 1982. On lava dome growth, with application to the 1979 lava extrusion of the Soufrière of St. Vincent. *Journal of Volcanology and Geothermal Research*, **14**, 199–222, [https://doi.org/10.1016/0377-0273\(82\)90062-2](https://doi.org/10.1016/0377-0273(82)90062-2)
- Johnston, A.D. and Stout, J.H. 1984. Development of orthopyroxene–Fe/Mg ferrite symplectites by continuous olivine oxidation. *Contributions to Mineralogy and Petrology*, **88**, 196–202, <https://doi.org/10.1007/BF00371423>
- Joseph, E.P., Camejo-Harry, M. *et al.* 2022. Responding to eruptive transitions during the 2020–2021 eruption of La Soufrière volcano, St. Vincent. *Nature Communications*, **13**, 4129, <https://doi.org/10.1038/s41467-022-31901-4>
- Kawai, N., Kume, S. and Sasajima, S. 1954. Magnetism of rocks and solid phase transformation in ferromagnetic minerals. *Proceedings of the Japan Academy*, **30**, 588–593, <https://doi.org/10.2183/pjab1945.30.588>
- Kelfoun, K., Santoso, A.B. *et al.* 2021. Growth and collapse of the 2018–2019 lava dome of Merapi volcano. *Bulletin of Volcanology*, **83**, 8, <https://doi.org/10.1007/s00445-020-01428-x>
- Khisina, N.R., Khramov, D.A., Kolosov, M.V., Kleschev, A.A. and Taylor, L.A. 1995. Formation of ferriolivine and magnesioferrite from Mg–Fe–olivine: Reactions and kinetics of oxidation. *Physics and Chemistry of Minerals*, **22**, <https://doi.org/10.1007/BF00202257>
- Khisina, N.R., Khramov, D.A., Kleschev, A.A. and Langer, K. 1998. Laihunitization as a mechanism of olivine oxidation. *European Journal of Mineralogy*, **10**, 229–238, <https://doi.org/10.1127/ejm/10/2/0229>
- Knafele, J., Filiberto, J. *et al.* 2019. The effect of oxidation on the mineralogy and magnetic properties of olivine. *American Mineralogist*, **104**, 694–702, <https://doi.org/10.2138/am-2019-6829>
- Kuno, H. 1966. Review of pyroxene relations in terrestrial rocks in the light of recent experimental works. *Mineralogical Journal*, **5**, 21–43, <https://doi.org/10.2465/minerj1953.5.21>
- Laeger, K., Halama, R., Hansteen, T., Savov, I.P., Murcia, H.F., Cortés, G.P. and Garbe-Schönberg, D. 2013. Crystallization conditions and petrogenesis of the lava dome from the ~900 years BP eruption of Cerro Machín Volcano, Colombia. *Journal of South American Earth Sciences*, **48**, 193–208, <https://doi.org/10.1016/j.jsames.2013.09.009>
- Lattard, D. 1995. Experimental evidence for the exsolution of ilmenite from titaniferous spinel. *American Mineralogist*, **80**, 968–981, <https://doi.org/10.2138/am-1995-9-1013>
- Lilova, K.I., Pearce, C.I., Gorski, C., Rosso, K.M. and Navrotsky, A. 2012. Thermodynamics of the magnetite–ulvöspinel (Fe_3O_4 – Fe_2TiO_4) solid solution. *American Mineralogist*, **97**, 1330–1338, <https://doi.org/10.2138/am.2012.4076>
- Lindsley, D.H. 1991. Experimental studies of oxide minerals. In: Lindsley, D.H. (ed.) *Oxide Minerals*. De Gruyter, 69–106, <https://doi.org/10.1515/9781501508684-006>
- Lindsley, D.H. and Andersen, D.J. 1983. A two-pyroxene thermometer. *Journal of Geophysical Research*, **88**, A887, <https://doi.org/10.1029/JB088iS02p0A887>
- Longhi, J. and Bertka, C.M. 1996. Graphical analysis of pigeonite–augite liquidus equilibria. *American Mineralogist*, **81**, 685–695, <https://doi.org/10.2138/am-1996-5-616>
- Ludlam, A.P., Frey, H.M. and Manon, M.R.F. 2018. Decompression and heating induced amphibole breakdown in effusive volcanism on Dominica, Lesser Antilles. Paper presented at the 53rd Annual GSA Northeastern Section Meeting, 311190, <https://doi.org/10.1130/abs/2018NE-311190>
- Macdonald, R., Hawkesworth, C.J. and Heath, E. 2000. The Lesser Antilles volcanic chain: a study in arc magmatism. *Earth-Science Reviews*, **49**, 1–76, [https://doi.org/10.1016/S0012-8252\(99\)00069-0](https://doi.org/10.1016/S0012-8252(99)00069-0)
- Mathez, E.A. 1984. Influence of degassing on oxidation states of basaltic magmas. *Nature*, **310**, 371–375, <https://doi.org/10.1038/310371a0>
- Matsumoto, K. and Geshi, N. 2021. Shallow crystallization of eruptive magma inferred from volcanic ash microtextures: a case study of the 2018 eruption of Shinmoedake volcano, Japan. *Bulletin of Volcanology*, **83**, 31, <https://doi.org/10.1007/s00445-021-01451-6>
- Miller, T.P. 1994. Dome growth and destruction during the 1989–1990 eruption of Redoubt Volcano. *Journal of Volcanology and Geothermal Research*, **62**, 197–212, [https://doi.org/10.1016/0377-0273\(94\)90034-5](https://doi.org/10.1016/0377-0273(94)90034-5)
- Moore, G. and Carmichael, I.S.E. 1998. The hydrous phase equilibria (to 3 kbar) of an andesite and basaltic andesite from western Mexico: constraints on water content and conditions of phenocryst growth. *Contributions to Mineralogy and Petrology*, **130**, 304–319, <https://doi.org/10.1007/s004100050367>
- Moore, H.C., Carey, R.J., Houghton, B.F., Jutzeler, M. and White, J.D.L. 2022. High-temperature oxidation of proximal basaltic pyroclasts, 1886 Tarawera, New Zealand. *Bulletin of Volcanology*, **84**, 46, <https://doi.org/10.1007/s00445-022-01549-5>
- Moseley, D. 1984. Symplectic exsolution in olivine. *American Mineralogist*, **69**, 139–153.
- Muan, A., Hauck, J. and Löfall, T. 1972. Equilibrium studies with a bearing on lunar rocks. *Lunar and Planetary Science Conference Proceedings*, **3**, 185.
- Mujin, M., Nakamura, M. and Miyake, A. 2017. Eruption style and crystal size distributions: Crystallization of groundmass nanolites in the 2011 Shinmoedake eruption. *American Mineralogist*, **102**, 2367–2380, <https://doi.org/10.2138/am-2017-6052CCBYNCND>
- Murch, A.P. and Cole, P.D. 2019. Using microlites to gain insights into ascent conditions of differing styles of volcanism at Soufrière Hills Volcano. *Journal of Volcanology and Geothermal Research*, **384**, 221–231, <https://doi.org/10.1016/j.jvolgeores.2019.07.022>
- Nakada, S., Zaennudin, A. *et al.* 2019. Growth process of the lava dome/flow complex at Sinabung Volcano

- during 2013–2016. *Journal of Volcanology and Geothermal Research*, **382**, 120–136, <https://doi.org/10.1016/j.jvolgeores.2017.06.012>
- Newhall, C.G. and Melson, W.G. 1983. Explosive activity associated with the growth of volcanic domes. *Journal of Volcanology and Geothermal Research*, **17**, 111–131, [https://doi.org/10.1016/0377-0273\(83\)90064-1](https://doi.org/10.1016/0377-0273(83)90064-1)
- Nicholls, I.A. and Ringwood, A.E. 1973. Effect of water on olivine stability in tholeiites and the production of silica-saturated magmas in the island-arc environment. *The Journal of Geology*, **81**, 285–300, <https://doi.org/10.1086/627871>
- Nickel, E.H. 1958. The composition and microtexture of an ulvöespinel-magnetite intergrowth [Quebec]. *The Canadian Mineralogist*, **6**, 191–199.
- Nitsan, U. 1974. Stability field of olivine with respect to oxidation and reduction. *Journal of Geophysical Research*, **79**, 706–711, <https://doi.org/10.1029/JB079i005p00706>
- Ogburn, S.E., Loughlin, S.C. and Calder, E.S. 2015. The association of lava dome growth with major explosive activity ($VEI \geq 4$): DomeHaz, a global dataset. *Bulletin of Volcanology*, **77**, 40, <https://doi.org/10.1007/s00445-015-0919-x>
- Pallister, J.S., Thornber, C.R. *et al.* 2008. Petrology of the 2004–2006 Mount St. Helens lava dome – implications for magmatic plumbing and eruption triggering. *USGS Professional Paper*, **1750**, Chapter 30, <https://doi.org/10.3133/pp175030>
- Petersen, N. 1970. Calculation of diffusion coefficient and activation energy of titanium in titanomagnetite. *Physics of the Earth and Planetary Interiors*, **2**, 175–178, [https://doi.org/10.1016/0031-9201\(70\)90005-1](https://doi.org/10.1016/0031-9201(70)90005-1)
- Preece, K., Barclay, J., Gertisser, R. and Herd, R.A. 2013. Textural and micro-petrological variations in the eruptive products of the 2006 dome-forming eruption of Merapi volcano, Indonesia: Implications for subsurface processes. *Journal of Volcanology and Geothermal Research*, **261**, 98–120, <https://doi.org/10.1016/j.jvolgeores.2013.02.006>
- Preece, K., Gertisser, R., Barclay, J., Charbonnier, S.J., Komorowski, J.-C. and Herd, R.A. 2016. Transitions between explosive and effusive phases during the cataclysmic 2010 eruption of Merapi volcano, Java, Indonesia. *Bulletin of Volcanology*, **78**, 54, <https://doi.org/10.1007/s00445-016-1046-z>
- Price, G.D. 1980. Exsolution microstructures in titanomagnetites and their magnetic significance. *Physics of the Earth and Planetary Interiors*, **23**, 2–12, [https://doi.org/10.1016/0031-9201\(80\)90078-3](https://doi.org/10.1016/0031-9201(80)90078-3)
- Price, G.D. 1981. Diffusion in the titanomagnetite solid solution series. *Mineralogical Magazine*, **44**, 195–200, <https://doi.org/10.1180/minmag.1981.044.334.13>
- Price, G.D. and Putnis, A. 1979. Oxidation phenomena in pleonaste bearing titanomagnetites. *Contributions to Mineralogy and Petrology*, **69**, 355–359, <https://doi.org/10.1007/BF00372261>
- Putirka, K.D. 2008. Thermometers and barometers for volcanic systems. *Reviews in Mineralogy and Geochemistry*, **69**, 61–120, <https://doi.org/10.2138/rmg.2008.69.3>
- Reagan, M.K., Gill, J.B., Malavassi, E. and Garcia, M.O. 1987. Changes in magma composition at Arenal volcano, Costa Rica, 1968?1985: Real-time monitoring of open-system differentiation. *Bulletin of Volcanology*, **49**, 415–434, <https://doi.org/10.1007/BF01046634>
- Ridolfi, F., Renzulli, A. and Puerini, M. 2010. Stability and chemical equilibrium of amphibole in calc-alkaline magmas: an overview, new thermobarometric formulations and application to subduction-related volcanoes. *Contributions to Mineralogy and Petrology*, **160**, 45–66, <https://doi.org/10.1007/s00410-009-0465-7>
- Ringwood, A.E. and Lovering, J.F. 1970. Significance of pyroxene-ilmenite intergrowths among kimberlite xenoliths. *Earth and Planetary Science Letters*, **7**, 371–375, [https://doi.org/10.1016/0012-821X\(69\)90052-1](https://doi.org/10.1016/0012-821X(69)90052-1)
- Sack, R.O. 1982. Spinel as petrogenetic indicators: Activity-composition relations at low pressures. *Contributions to Mineralogy and Petrology*, **79**, 169–186, <https://doi.org/10.1007/BF01132886>
- Saito, T., Ishikawa, N. and Kamata, H. 2004a. Iron–titanium oxide minerals in block-and-ash-flow deposits: implications for lava dome oxidation processes. *Journal of Volcanology and Geothermal Research*, **138**, 283–294, <https://doi.org/10.1016/j.jvolgeores.2004.07.006>
- Saito, T., Ishikawa, N. and Kamata, H. 2004b. *Magnetic Petrology of Unzen Volcano, Japan: Implications for Lava Dome Oxidation Processes*. Annual Report of the Disasters Prevention Research Institute, Kyoto University, **47**.
- Saito, T., Ishikawa, N. and Kamata, H. 2007. Magnetic petrology of the 1991–1995 dacite lava of Unzen volcano, Japan: Degree of oxidation and implications for the growth of lava domes. *Journal of Volcanology and Geothermal Research*, **164**, 268–283, <https://doi.org/10.1016/j.jvolgeores.2007.05.015>
- Sato, M. and Wright, T.L. 1966. Oxygen fugacities directly measured in magmatic gases. *Science (New York, NY)*, **153**, 1103–1105, <https://doi.org/10.1126/science.153.3740.1103>
- Schiavi, F., Walte, N. and Keppler, H. 2009. First in situ observation of crystallization processes in a basaltic-andesitic melt with the moissanite cell. *Geology*, **37**, 963–966, <https://doi.org/10.1130/G30087A.1>
- Speidel, D.H. 1967. Phase equilibria in the system $MgO-FeO-Fe_2O_3$: The 1300°C isothermal section and extrapolations to other temperatures. *Journal of the American Ceramic Society*, **50**, 243–248, <https://doi.org/10.1111/j.1151-2916.1967.tb15096.x>
- Stinton, A. 2023. Growth and evolution of the lava dome and coulée during the 2020–21 eruption of La Soufrière, St Vincent. *Geological Society, London, Special Publications*, **539**, <https://doi.org/10.1144/SP539-2022-304>
- Swanson, D.A., Dzuris, D. *et al.* 1987. Growth of the lava dome at Mount St. Helens, Washington, (USA), 1981–1983. *Geological Society of America Special Papers*, **212**, 1–16, <https://doi.org/10.1130/SPE212-p1>
- Tan, W., Liu, P., He, H., Wang, C.Y. and Liang, X. 2016. Mineralogy and origin of exsolution in Ti-rich magnetite from different magmatic Fe–Ti oxide-bearing intrusions. *The Canadian Mineralogist*, **54**, 539–553, <https://doi.org/10.3749/canmin.1400069>
- Turner, M.B., Cronin, S.J., Stewart, R.B., Bebbington, M. and Smith, I.E.M. 2008. Using titanomagnetite textures to elucidate volcanic eruption histories. *Geology*, **36**, 31, <https://doi.org/10.1130/G24186A.1>

- Turnock, A.C. and Eugster, H.P. 1962. Fe–Al oxides: phase relationships below 1,000 C. *Journal of Petrology*, **3**, 533–565, <https://doi.org/10.1093/petrology/3.3.533>
- Ueda, H., Shibuya, T., Sawaki, Y., Shozugawa, K., Makabe, A. and Takai, K. 2021. Chemical nature of hydrothermal fluids generated by serpentinization and carbonation of komatiite: implications for H₂-rich hydrothermal system and ocean chemistry in the early Earth. *Geochemistry, Geophysics, Geosystems*, **22**, <https://doi.org/10.1029/2021GC009827>
- Ueki, K., Inui, M., Matsunaga, K., Okamoto, N. and Oshio, K. 2020. Oxidation during magma mixing recorded by symplectites at Kusatsu–Shirane Volcano, Central Japan. *Earth, Planets and Space*, **72**, 68, <https://doi.org/10.1186/s40623-020-01192-4>
- Utami, S.B., Andujar, J., Costa, F., Scaillet, B. and Humaida, H. 2021. The role of magma storage conditions and excess fluids in the effusive to explosive eruption styles [Preprint]. *ESS Open Archive*, <https://doi.org/10.1002/essoar.10508062.1> [last accessed 30 May 2023]
- Venezky, D.Y. and Rutherford, M.J. 1999. Petrology and Fe–Ti oxide reequilibration of the 1991 Mount Unzen mixed magma. *Journal of Volcanology and Geothermal Research*, **89**, 213–230, [https://doi.org/10.1016/S0377-0273\(98\)00133-4](https://doi.org/10.1016/S0377-0273(98)00133-4)
- Vincent, E.A., Wright, J.B., Chevallier, R. and Mathieu, S. 1957. Heating experiments on some natural titaniferous magnetites. *Mineralogical Magazine and Journal of the Mineralogical Society*, **31**, 624–655, <https://doi.org/10.1180/minmag.1957.31.239.03>
- Voight, B., Constantine, E.K., Siswondjono, S. and Torley, R. 2000. Historical eruptions of Merapi Volcano, Central Java, Indonesia, 1768–1998. *Journal of Volcanology and Geothermal Research*, **100**, 69–138, [https://doi.org/10.1016/S0377-0273\(00\)00134-7](https://doi.org/10.1016/S0377-0273(00)00134-7)
- Von Gruenewaldt, G., Klemm, D.D., Henckel, J. and Dehm, R.M. 1985. Exsolution features in titanomagnetites from massive magnetite layers and their host rocks of the upper zone, eastern Bushveld Complex. *Economic Geology*, **80**, 1049–1061, <https://doi.org/10.2113/gsecongeo.80.4.1049>
- Walker, G.P.L., Huntingdon, A.T., Sanders, A.T. and Dinsdale, J.L. 1973. Lengths of lava flows [and discussion]. *Philosophical Transactions of the Royal Society of London Series A, Mathematical and Physical Sciences*, **274**, 107–118.
- Weber, G., Blundy, J. *et al.* 2023. Petrology of the 2020–21 effusive to explosive eruption of La Soufrière volcano, St Vincent: insights into plumbing system architecture and magma assembly mechanism. *Geological Society, London, Special Publications*, **539**, <https://doi.org/10.1144/SP539-2022-177>
- Wells, P.R.A. 1977. Pyroxene thermometry in simple and complex systems. *Contributions to Mineralogy and Petrology*, **62**, 129–139, <https://doi.org/10.1007/BF00372872>
- Woermann, E., Brezney, B. and Muan, A. 1969. Phase equilibria in the system MgO–iron oxide – TiO₂ in air. *American Journal of Science*, **267**, 463–479.
- Zharinov, N.A. and Demyanchuk, Y.V. 2013. Large explosive eruptions of Shiveluch volcano, Kamchatka resulting in partial destruction of the extrusive dome (February 28, 2005 and October 27, 2010). *Journal of Volcanology and Seismology*, **7**, 131–144, <https://doi.org/10.1134/S0742046313020061>